HEALTH AND MEDICINE

Immunomodulatory multicellular scaffolds for tendon-to-bone regeneration

Lin Du[1,2]†, Jinfu Wu[1,2]†, Yahui Han[1,2], Chengtie Wu[1,2]*

Limited motor activity due to the loss of natural structure impedes recovery in patients suffering from tendon-to-bone injury. Conventional biomaterials focus on strengthening the regenerative ability of tendons/bones to restore natural structure. However, owing to ignoring the immune environment and lack of multi-tissue regenerative function, satisfactory outcomes remain elusive. Here, combined manganese silicate (MS) nanoparticles with tendon/bone-related cells, the immunomodulatory multicellular scaffolds were fabricated for integrated regeneration of tendon-to-bone. Notably, by integrating biomimetic cellular distribution and MS nanoparticles, the multicellular scaffolds exhibited diverse bioactivities. Moreover, MS nanoparticles enhanced the specific differentiation of multicellular scaffolds via regulating macrophages, which was mainly attributed to the secretion of *PGE2* in macrophages induced by Mn ions. Furthermore, three animal results indicated that the scaffolds achieved immunomodulation, integrated regeneration, and function recovery at tendon-to-bone interfaces. Thus, the multicellular scaffolds based on inorganic biomaterials offer an innovative concept for immunomodulation and integrated regeneration of soft/hard tissue interfaces.

INTRODUCTION

The musculoskeletal system, especially the tendon-to-bone interface, plays an important role in human motor function (*1*). The tendon-to-bone interface is where the tendon inserts into the bone. It is composed of tendon, fibrocartilage, and bone, and there are gradual and continuous transitions between these adjacent tissues (*2*–*4*). These interfaces with unique structures allow for efficient relief of stress concentrations (*5*, *6*). When injury occurs, due to the complex physiology and poor regenerative capacity, clinical surgical treatments tend to form scar tissues rather than natural interfaces, leading to a high probability of reinjury (*5*, *7*). In the field of tendon-to-bone injury repair, conventional biomaterials have a single biological activity, which can only promote osseointegration or tendon maturation (*8*–*11*). Recently, some biphasic scaffolds or multiphasic scaffolds have been developed to act simultaneously on multiple tissues at the interface (*12*, *13*). For example, Yang *et al.* (*14*) constructed a gradient bimetallic ion–based hydrogel through cross-linking sulfhydryl groups with copper (Cu) and zinc (Zn) ions. Besides, Zhu *et al.* (*13*) designed a triphasic scaffold with arrayed channels in the upper layer, mineral compositional gradients in the middle layer, and mineralized inverse opal region in the bottom layer. To more realistically simulate the interface components, Tang *et al.* (*15*) fabricated a gradient book-type triphasic scaffold which consisted of decellularized tendon, fibrocartilage, and bone tissues. Although the healing effect of tendon-to-bone injuries has been improved, the formation of scar structures at the interface and limited motor function is still inevitable (*1*, *5*). One of the major reasons for this is that most of the biomaterials developed by researchers only focus on augmenting the biological functions directly related to tendon-to-bone (*16*, *17*), such as osteogenic differentiation or tenogenic differentiation, while ignoring the effect of the

three-dimensional (3D) microenvironment surrounding the injury site, especially inflammatory responses triggered by immune cells in vivo (*12*, *18*, *19*). Among various immune cells, macrophages have received increasing attention in tendon-to-bone injury since they are closely associated with tendon fibrosis (*20*, *21*). Better histological and biomechanical properties are achieved by reducing M1 macrophage accumulation and inducing M2 macrophage polarization at the tendon-to-bone interface according to previous studies (*22*, *23*). Unfortunately, due to high muscle loading and stress, the conversion of M1 and M2 in macrophages tends to be delayed at the tendon-to-bone interface, which results in chronic inflammation (*21*, *24*). As is known to all, the immune environment usually determines the outcome of tissue damage repair (*25*–*27*). An appropriate inflammatory response facilitates the initiation of tissue repair, whereas excessive inflammation can, in turn, impede the progression of tissue repair and stimulate the development of pathological fibrosis/scar structures at the site of injury, thereby depriving the biomaterial of its intended function (*25*, *28*–*30*). Hence, in addition to the ability to induce the regeneration of multiple tissues, ideal tendon-to-bone tissue engineering scaffolds need to fully take full account of the immunomodulatory functions of the 3D biological microenvironment.

In recent years, 3D multicellular scaffolds based on bioprinting technology have been widely used in the regeneration of complex tissues (*31*–*33*). These multicellular scaffolds enable the regulation of cell-cell and cell-surrounding environment interactions by personalizing the composition of bioinks as needed (*34*–*36*). Moreover, the simulation of composition and structure on complex tissues can also be achieved easily by the construction of these multicellular scaffolds, which has a positive effect on microstructure restoration of the tendon-to-bone interface (*37*, *38*). Thus, these multicellular scaffolds inspire the construction of ideal tendon-to-bone tissue engineering scaffolds.

To achieve immunomodulatory and integrated regeneration, the design of bioinks is critical. In our previous work, it has been found that silicate bioceramics are able to create a suitable physiological microenvironment through the release of bioactive ions, thus affecting cellular behaviors and cross-talk among cells (*39*–*41*). Silicon (Si)

[1]State Key Laboratory of High Performance Ceramics and Superfine Microstructure Shanghai Institute of Ceramics, Chinese Academy of Sciences, 1295 Dingxi Road, Shanghai 200050, P. R. China. [2]Center of Materials Science and Optoelectronics Engineering, University of Chinese Academy of Sciences, 19A Yuquan Road, Beijing 100049, P. R. China.
*Corresponding author. Email: chengtiewu@mail.sic.ac.cn
†These authors contributed equally to this work.

element, one of the constituent elements of bone and connective tissue, has been used to repair soft and hard tissue injury (*42, 43*) In addition, the manganese (Mn) element is an important cofactor for several key enzymes in living organisms (*44*). It has been reported that Mn deficiency results in impairment of cell adhesion, proliferation, and differentiation (*45*). Furthermore, Mn ions display a positive effect on angiogenesis which is essential for osteogenic and tenogenic processes (*36, 46, 47*). Notably, Mn-containing biomaterials also have been confirmed to inhibit the expression of typical pro-inflammatory genes, such as *TNF-α*, *IL-6*, *OSM*, and *IL-1β*. Furthermore, Mn-containing biomaterials could enhance the expression of anti-inflammatory genes (*IL-10*, *Arg-1*, *CD206*, and *VEGF*) in macrophages (*36*). Hence, given the properties of Si and Mn as described above, it is reasonable to speculate that bioinks incorporated Mn-Si biomaterials have great potential to endow the multicellular scaffolds with immunomodulatory and integrated regenerative functions for tendon-to-bone injury.

Here, we successfully developed a multicellular scaffold based on manganese silicate (MS) nanoparticles for immunomodulation and integrated regeneration of tendon-to-bone injury. Specifically, tendon stem/progenitor cells (TSPCs) and bone marrow mesenchymal stem cells (BMSCs) were distributed in the scaffold in a layered manner, which realized the simulation of tendon-to-bone interfaces (Fig. 1). Benefiting from multicellular distribution and MS nanoparticles, the multicellular scaffolds showed promising potential in immunomodulatory capacity and integrated tendon-to-bone regeneration in vitro. Immunomodulation, the restoration of interfacial microstructure, and function recovery were simultaneously achieved by implanting of the multicellular scaffolds into rabbit and rat rotator cuff tears (RCTs). Subsequently, the multicellular scaffolds based on MS nanoparticles also were implanted into macrophage-depleted rats to further reveal

Fig. 1. Schematic illustration of the immunomodulatory multicellular scaffolds based on MS nanoparticles for integrated tendon-to-bone regeneration. The multicellular scaffolds based on MS nanoparticles were fabricated through the spatial distribution of tendon stem/progenitor cells (TSPCs) and bone marrow mesenchymal stem cells (BMSCs) using 3D bioprinting, which achieved simulation of the tendon-to-bone interface. Moreover, MS nanoparticles were incorporated into the multicellular scaffolds for conferring immunomodulatory and integrated regenerative functions to the scaffolds. After being implanted into a rotator cuff tear (RCT), the multicellular scaffolds containing MS nanoparticles could induce the regeneration of tendon-to-bone interfaces in vivo.

the role of immunomodulatory processes in the specific differentiation of scaffolds. Furthermore, the mechanism of Mn ions in promoting the regeneration of tendon-to-bone interfaces through immunomodulation was intensively investigated. In summary, the construction of immunomodulatory multicellular scaffolds offers a promising strategy for the integrated regeneration of soft-to-hard tissue interfaces.

RESULTS AND DISCUSSION
Construction and characterization of 3D bioprinted multicellular scaffolds

First, the MS nanoparticles and gelatin methacryloyl (GelMA) were synthesized according to previous studies (*36, 48*). Scanning transmission electron microscope (STEM) images demonstrated that the MS nanoparticles were hollow spheres with diameters close to 100 nm (Fig. 2A). Besides, Mn and Si elements were uniformly distributed in MS nanoparticles according to energy-dispersive spectroscopy. The x-ray diffraction (XRD) pattern indicated that MS nanoparticles were indexed into $(Mn_2O_3)_3MnSiO_3$ (PDF #41-1367) (Fig. 2B). Thus, the above results confirmed the successful preparation of MS nanoparticles. Next, MS nanoparticles were incorporated into GelMA hydrogel at different mass ratios (0, 2, 5, 10, and 15%) to create a series of composite inks named GelMA, GelMA-2MS, GelMA-5MS, GelMA-10MS, and GelMA-15MS, respectively (Fig. 2C). As shown in Fig. 2D, the printability analysis showed that the approximate degree of the actual values to the theoretical values in all groups was positively correlated with the concentrations of incorporated MS nanoparticles, suggesting that the incorporation of MS nanoparticles improved the printability of pure GelMA hydrogel. Subsequently, to simulate the tendon-to-bone interface in terms of the layered structure and cellular composition, BMSCs and TSPCs were added into composite inks to obtain bilayered multicellular scaffolds via the 3D bioprinting technique. Judging from the CCK-8 assay, the cells in GelMA, GelMA-2MS, GelMA-5MS, and GelMA-10MS groups proliferated significantly over time, while those in the GelMA-15MS group showed a weaker trend of cell proliferation. Besides, the number of cells in the GelMA-15MS group was the least compared to the other groups on day 14 (Fig. 2E). Thus, given the poor biocompatibility caused by a high concentration of MS nanoparticles, GelMA-15MS was not considered in the subsequent experiments. Next, the elastic modulus was calculated on the basis of the slope of the curve 0 to 10% strain, and the results showed that the elastic modulus of the scaffolds was significantly enhanced with the increase of MS nanoparticle content (fig. S2, A and B). Then, through the SEM images of GelMA-MS, it was observed that the incorporation of MS nanoparticles did not destroy the porous structure of GelMA hydrogel (fig. S2C). Furthermore, by observation of the live/dead images, both BMSCs and TSPCs maintained high viability in all groups during 21 days of culture (Fig. 2F and fig. S3). Moreover, the confocal laser scanning microscopy (CLSM) images showed that BMSCs (red fluorescence) were in the lower layer and TSPCs (green fluorescence) were in the upper layer during the culture period (Fig. 2G), indicating that the multicellular scaffolds had a biomimetic structure similar to tendon-to-bone and could remain structural stability for 14 days. In addition, according to the ionic release curves, the Mn and Si ions were gradually released into the culture medium, and the concentration of released Mn and Si ions increased with the rising of MS concentration (fig. S4, A and B). Therefore, these results verified the successful construction of multicellular scaffolds
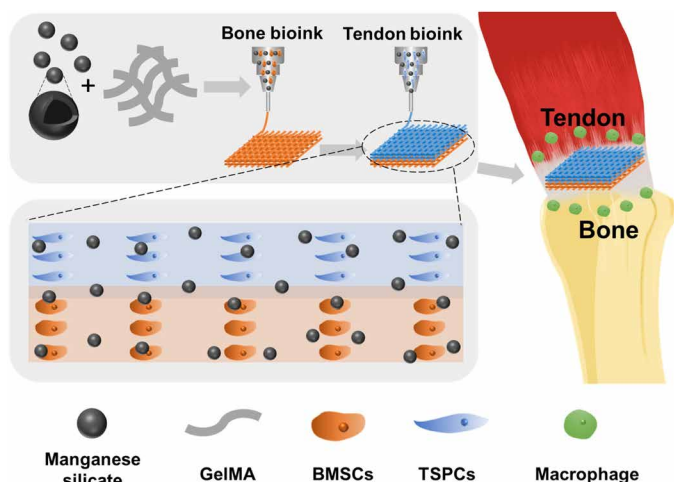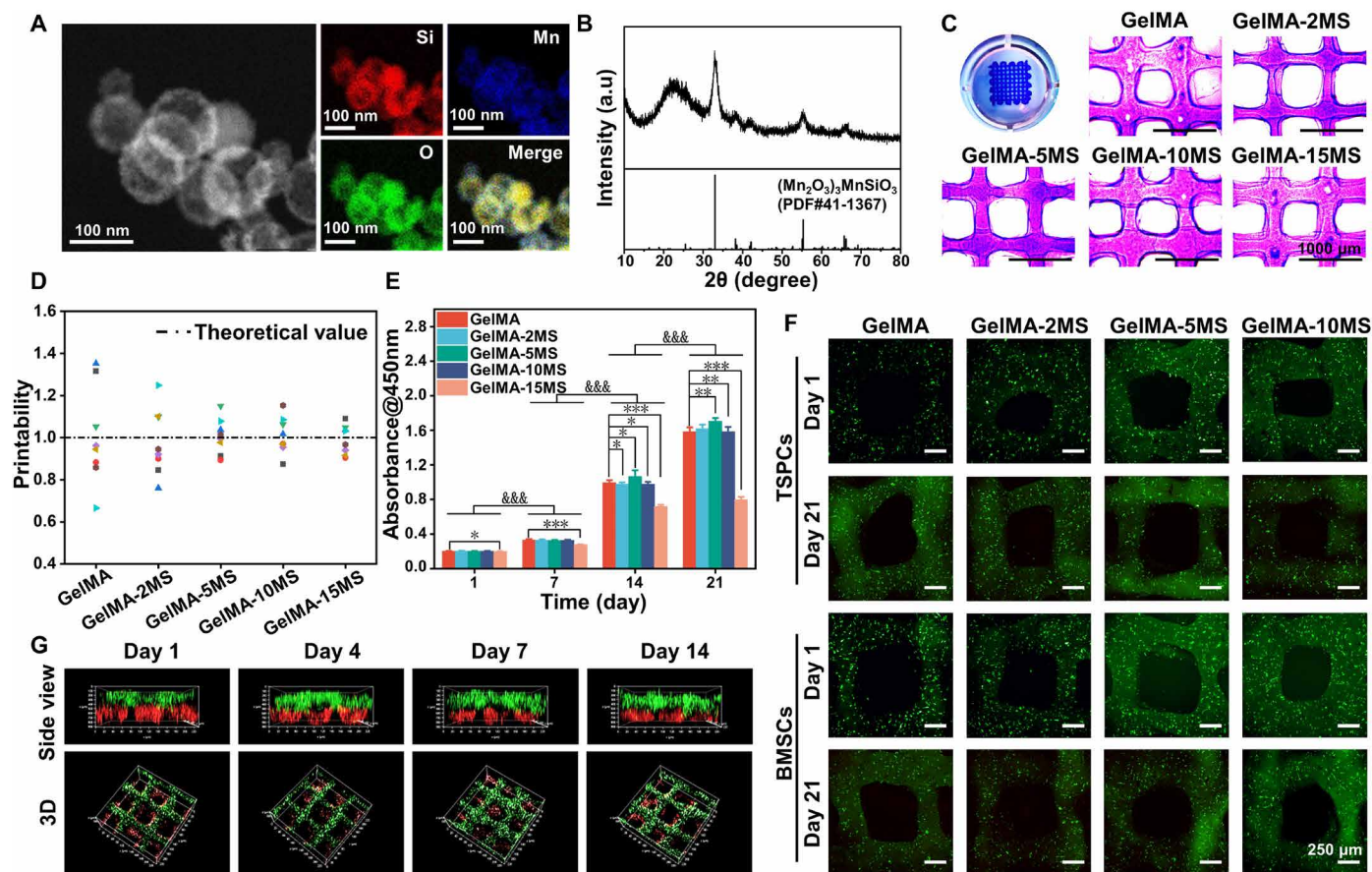
Fig. 2. Characterization of MS nanoparticles, bioinks containing MS nanoparticles, and the multicellular scaffolds based on MS nanoparticles. (**A**) Scanning transmission electron microscope images of MS nanoparticles. (**B**) X-ray diffraction of MS nanoparticles. a.u., arbitrary units. (**C**) The photographs and (**D**) printability of bioinks containing different concentrations of MS nanoparticles ($n = 8$). (**E**) The proliferation activity of cells in multicellular scaffolds during 21 days of culture ($n = 6$). *$P < 0.05$, **$P < 0.01$, and ***$P < 0.001$ (comparison of different groups at the same time point). &&&$P < 0.001$ (comparison of the same group at different time points). (**F**) Live/dead staining images of TSPCs and BMSCs in multicellular scaffolds after being cultured for 1 and 21 days. (**G**) Confocal laser scanning microscopy (CLSM) images of the spatial distribution of BMSCs (red fluorescence) and TSPCs (green fluorescence) in multicellular scaffolds during 14 days of culture. The multicellular scaffolds based on MS nanoparticles supported the proliferation and survival of internal cells and maintained a stable bilayered structure during culture.

incorporated MS nanoparticles with structural stability, biocompatibility, and bioactive ion release properties.

The osteogenic and tenogenic differentiation of the multicellular scaffolds containing MS nanoparticles

To explore the effect of MS nanoparticles on the specific differentiation of BMSCs and TSPCs within the scaffolds, osteogenic and tenogenic markers were detected. First, the early osteogenic marker (alkaline phosphatase, ALP), the late osteogenic marker (mineralized nodule), and the osteogenic protein (OPN) were analyzed separately to evaluate the ability of MS nanoparticles on the osteogenic differentiation of BMSCs in the bottom layer of scaffolds. The ALP staining and the corresponding quantitative analysis of BMSCs inside the scaffolds containing various concentrations of MS nanoparticles were performed on days 7 and 14, respectively. As shown in Fig. 3 (A, C, and D), it was found that GelMA-2MS and GelMA-5MS could enhance the ALP activity of BMSCs on days 7 and 14. Meanwhile, GelMA-10MS had no significant effect on ALP activity at day 7 but increased ALP activity at day 14. Therefore, the appropriate

concentration of MS nanoparticles, especially GelMA-2MS and GelMA-5MS, had a more significant effect on increasing the ALP activity of BMSCs within scaffolds. Next, the mineralized nodule was examined by alizarin red S (ARS) staining and the semiquantitative analysis was performed after calcium nodules were dissolved (Fig. 3, B, E, and F). Compared with the GelMA group, GelMA-2MS, GelMA-5MS, and GelMA-10MS all promoted the formation of mineralized nodules at day 14. Among them, GelMA-5MS produced the highest number of mineralized nodules on day 14 but was not significantly different from GelMA-2MS. In addition, the content of mineralized nodules generated in all groups increased with the extension of culture time. Notably, GelMA-5MS still maintained the highest content of mineralized nodules at day 21. Last, to further detect the expression of osteogenic marks in different groups, the immunofluorescence staining of OPN protein was performed. Figure 3H showed that the OPN expression level of BMSCs in multicellular scaffolds containing MS nanoparticles was all higher than in pure GelMA scaffolds. According to the semiquantitative statistics, GelMA-5MS had the highest OPN protein expression (Fig. 3J).
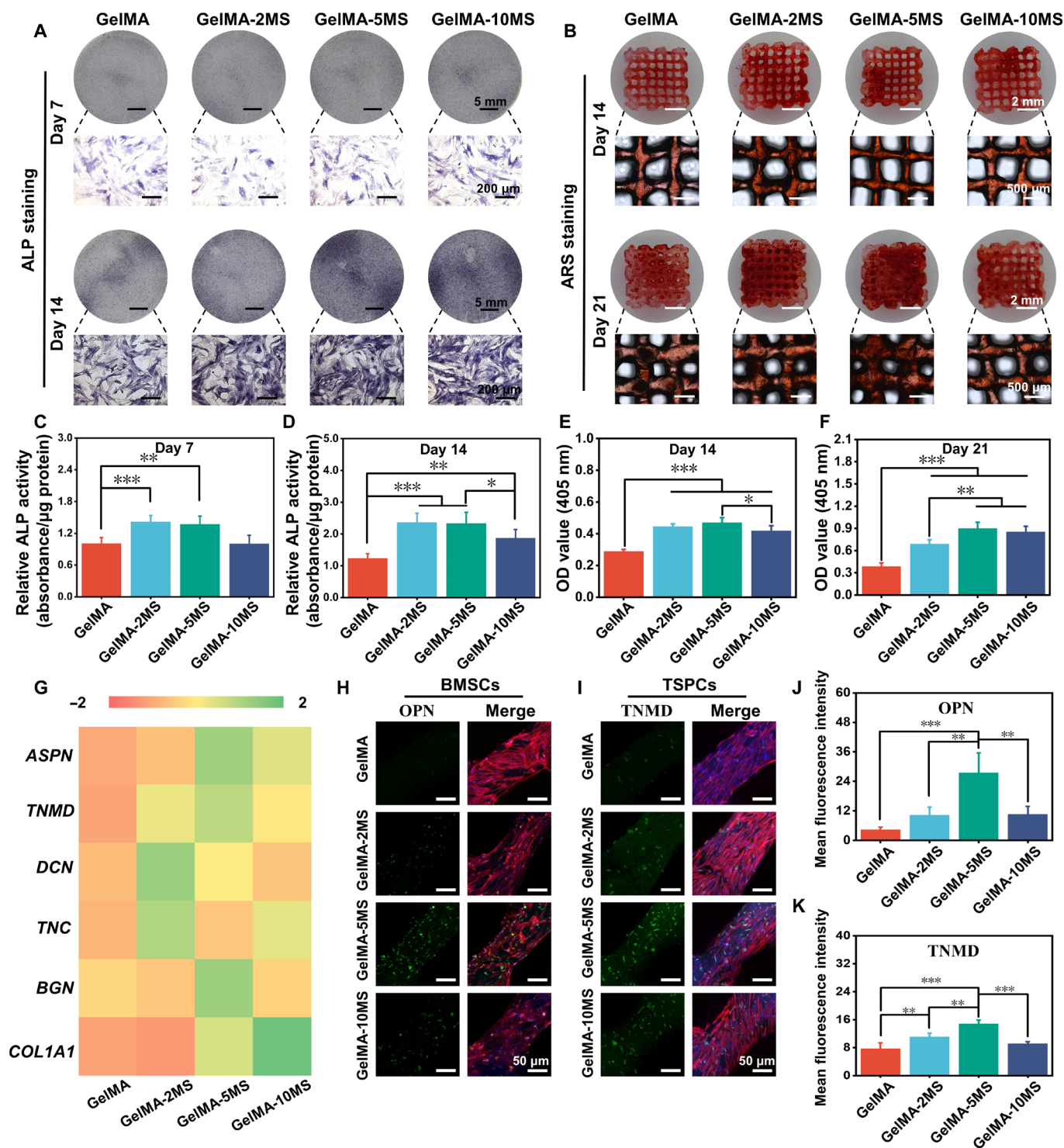
Fig. 3. The osteogenic differentiation of BMSCs and tenogenic differentiation of TSPCs encapsulated in the multicellular scaffolds. (**A**) The ALP staining of multicellular scaffolds containing different concentrations of MS nanoparticles after being cultured for 7 and 14 days. (**B**) The alizarin red S (ARS) staining of multicellular scaffolds containing different concentrations of MS nanoparticles after being cultured for 14 and 21 days. The relative quantitative analysis of ALP staining after (**C**) 7 and (**D**) 14 days of culture and ARS staining after (**E**) 14 and (**F**) 21 days of culture ($n = 5$). (**G**) The tenogenic differentiation–related cytokines (*ASPN*, *TNMD*, *DCN*, *TNC*, *BGN*, and *COL1A1*) secretion of TSPCs in multicellular scaffolds with different concentrations of MS nanoparticles during the culture of 14 days ($n = 3$). The expression of (**H**) OPN protein in BMSCs and (**I**) TNMD protein in TSPCs within multicellular scaffolds containing different concentrations of MS nanoparticles. The corresponding semiquantitative analysis of (**J**) OPN and (**K**) TNMD protein expression ($n = 3$). *$P < 0.05$, **$P < 0.01$, and ***$P < 0.001$. MS nanoparticles held the significant ability to simultaneously induce tenogenic differentiation of TSPCs and osteogenic differentiation of BMSCs in the multicellular scaffolds.

Then, as for the tenogenic differentiation of TSPCs in the upper layer of multicellular scaffolds, the secretion level of tenogenic differentiation–related cytokines (*ASPN*, *TNMD*, *DCN*, *TNC*, *BGN*, and *COL1A1*) was detected by enzyme-linked immunosorbent assay (ELISA) assay. *COL1A1* is a major gene encoding type I collagen which is the most abundant collagen in tendon tissue, accounting for 97% of the collagen content (*49*). Moreover, *tenomodulin* (*TNMD*), a member of type II transmembrane glycoproteins, can regulate tendon cell proliferation and participate in collagen fiber maturation (*50*, *51*). Besides, *decorin* (*DCN*) and *biglycan* (*BGN*) belong to small leucine-rich proteoglycans which can promote the normal development of collagen fiber structure within tendon tissues (*52*, *53*). *Asporin* (*ASPN*) is an extracellular matrix (ECM) protein and is closely associated with *BGN* and *DCN* (*54*). In addition, *tenascin-C* (*TNC*), a hexameric ECM glycoprotein, is present in large quantities around the cells and collagen fibers of the Achilles tendon and may affect tissue elasticity (*55*). Compared with the pure GelMA group, the multicellular scaffolds containing MS nanoparticles (GelMA-2MS, GelMA-5MS, and GelMA-10MS) all secreted more tendon-related cytokines. Specifically, GelMA-10MS secreted the most *COL1A1*; GelMA-2MS secreted the most *DCN* and *TNC*; and GelMA-5MS secreted the highest amount of *ASPN*, *TNMD*, and *BGN* (Fig. 3G). Moreover, the expression of *TNMD* protein in TSPCs was explored by immunofluorescence staining (Fig. 3, I and K). It was revealed that the expression level of *TNMD* in the GelMA-2MS and GelMA-5MS groups was significantly higher than those in the GelMA group, which was consistent with the above ELISA results.

Together, the multicellular scaffolds based on MS nanoparticles exhibited osteogenic and tenogenic differentiation activities. Notably, GelMA-5MS showed an optimal ability to induce the osteogenic differentiation of BMSCs and the tenogenic differentiation of TSPCs within scaffolds. Hence, GelMA-5MS was chosen for the further experiments.

Immunomodulation and tissue function recovery induced by multicellular scaffolds in rat RCT

To explore the immunomodulation and promotion of shoulder function restoration of the multicellular scaffolds containing MS nanoparticles in vivo, RCT of rats was established (Fig. 4A). First, the early host immune response induced by GelMA-cells and GelMA-cells–MS in the damaged region was examined. On postoperative days 4, 7, and 14, the immune cell types that responded to the implantation of scaffolds in damaged regions were investigated in different groups. Notably, the results of immunofluorescence staining and semiquantitative analysis indicated that the highest number of macrophages, rather than other immune cells, including leukocytes (CD18^{+} cells), T cells (CD4^{+} cells), and B cells (CD21+ cells), surrounded the scaffolds during the 14 days after surgery (fig. S5). Besides, there was no significant decrease in the number of macrophages over time within 14 days. Then, the immunofluorescence staining of Arg-1 (M2 marker) and CD68 was performed to identify the phenotype of macrophages surrounding the scaffold (Fig. 4B). The quantitative analysis revealed that the ratio of M2 phenotype macrophages was low both in GelMA-cells and GelMA-cells–MS around the defects at day 4, and there was no significant difference between these two groups. However, on days 7 and 14 after surgery, the number of M2 macrophages (Arg-1^{+}/CD68^{+} cells) was higher in the GelMA-cells–MS group than in the GelMA-cells group (Fig. 4C). These findings proved that GelMA-cells–MS successfully promoted the macrophage

M2 polarization and created an anti-inflammatory immune microenvironment in vivo.

The function recovery of damaged shoulder joints is one of the primary purposes of RCT repair. Gait analysis and biomechanical tests were able to provide quantifiable behavioral data on animal movements and interfacial mechanical strength, which could assess the functional recovery of RCT (*56*). The gait analysis was conducted through the acquisition of pawprints by the device shown in fig. S6A. To more comprehensively analyze the repair effect of live cells and MS nanoparticles in scaffolds, the rats that received sham operation without scaffold implantation were used as control (Blank), and non-operated, age-matched healthy rats were also considered (Normal). At each particular time point (1, 4, and 8 weeks), the spatial parameters (stride length, stride width, and step length), and paw parameters (paw length and toe spread) were collected, respectively (fig. S6B). As observed from Fig. 4 (D to F) and fig. S7, all the rats that underwent operation displayed gait abnormalities and their parameters showed no significant difference among these groups after 1 week of surgery. Moreover, there was a tendency for all rats to recover over time. Among them, the stride length in the Blank group was improved from week 4 to week 8 and the toe spread was getting better from week 1 to week 4. Besides, the stride width and step length in GelMA-cells were improved from week 1 to week 4, while there was no significant difference from week 4 to week 8. Meanwhile, GelMA-cells also improved the stride length from week 4 to week 8. Encouragingly, the stride width and length of rats treated by GelMA-cells–MS scaffolds both recovered significantly and tended to be normal from week 1 to week 8. In addition, GelMA-cells–MS scaffolds significantly facilitated the restoration of paw length from week 4 to week 8. Comparing of different groups at 4 weeks, the recovery degree of pawprints was better in the GelMA-cells and GelMA-cells–MS groups than in the Blank group, which was also evidenced by the asymmetry of other parameters after treatment of 4 weeks. Notably, the degree of difference further increased at 8 weeks postoperatively, and the GelMA-cells–MS group showed superiority in all parameters. Furthermore, all parameter values of GelMA-cells–MS were closest to those of the normal group, indicating that the excellent repair performance was induced by GelMA-cells–MS. In addition, the videos at different time points corroborated the above results (movie S1). Afterward, the biomechanical test was applied to evaluate the healing quality of the rotator cuff (Fig. 4G). As shown in Fig. 4H, the ultimate failure load of the GelMA-cells–MS was markedly higher than that of the GelMA-cells and Blank groups, and there was no significant difference between the GelMA-cells–MS group and the Normal group. According to the stiffness analysis, although the stiffness of the surgically operated rotator cuff did not recover to the normal level, the GelMA-cells–MS group still showed enhanced stiffness compared with the Blank group (Fig. 4I). Hence, these results indicated that GelMA-cells–MS achieved the immunomodulation and promoted the restoration of motion function and mechanical performance at the tendon-to-bone in vivo.

Histological structure restoration induced by multicellular scaffolds in rabbit RCT

Encouraged by the excellent motion function, Micro–computed tomography (micro-CT) and histological analysis were performed to further assess the tissue repair meticulously in rabbits RCT (Fig. 5A). First, the damaged humerus was reconstructed by micro-CT. According to Fig. 5B, significant unhealing cortical bones were observed in the
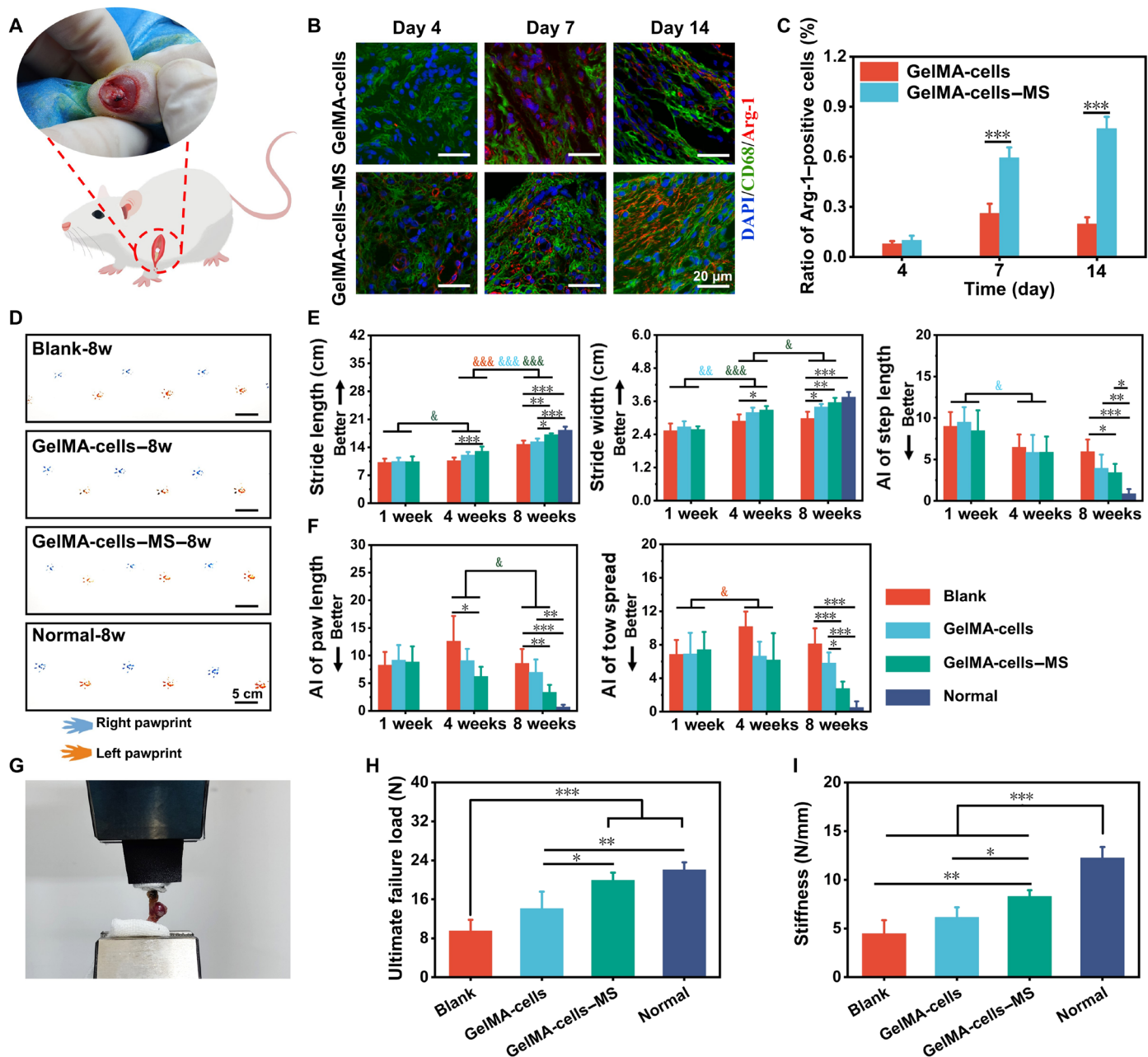
Fig. 4. The multicellular scaffolds based on MS nanoparticles achieved immunomodulation and induced functional restoration in rat RCT. (**A**) The schematic diagram of rat RCT. (**B**) Representative immunofluorescence staining images of M2 polarization–related markers (Arg-1/CD68) in macrophages surrounding the implanted scaffolds on days 4, 7, and 14 after surgery. (**C**) Quantification of the number ratio of Arg-1 positive macrophages to total macrophages ($n = 4$). (**D**) Representative pawprints of different groups at 8 weeks postoperatively. Quantification of rat (**E**) spatial gait parameters (from left to right: stride length, stride width, and step length) and (**F**) paw parameters (from left to right: paw length and toe spread) in different groups at 1, 4, and 8 weeks after surgery ($n = 4$). *$P < 0.05$, **$P < 0.01$, and ***$P < 0.001$ (comparison of different groups at the same time point). &$P < 0.05$, &&$P < 0.01$, and &&&$P < 0.001$ (comparison of the same group at different time points. Red: Blank group; blue: GelMA-cells group; green: GelMA-cells-MS group). (**G**) The representative biomechanical test image of repaired rat rotator cuffs ($n = 4$). (**H**) The ultimate failure load and (**I**) stiffness of treated rotator cuffs in different groups at 8 weeks postoperatively ($n = 4$). *$P < 0.05$, **$P < 0.01$, ***$P < 0.001$. The multicellular scaffolds based on MS nanoparticles polarized in vivo macrophages toward M2 phenotype and enhanced functional recovery in rat RCT.
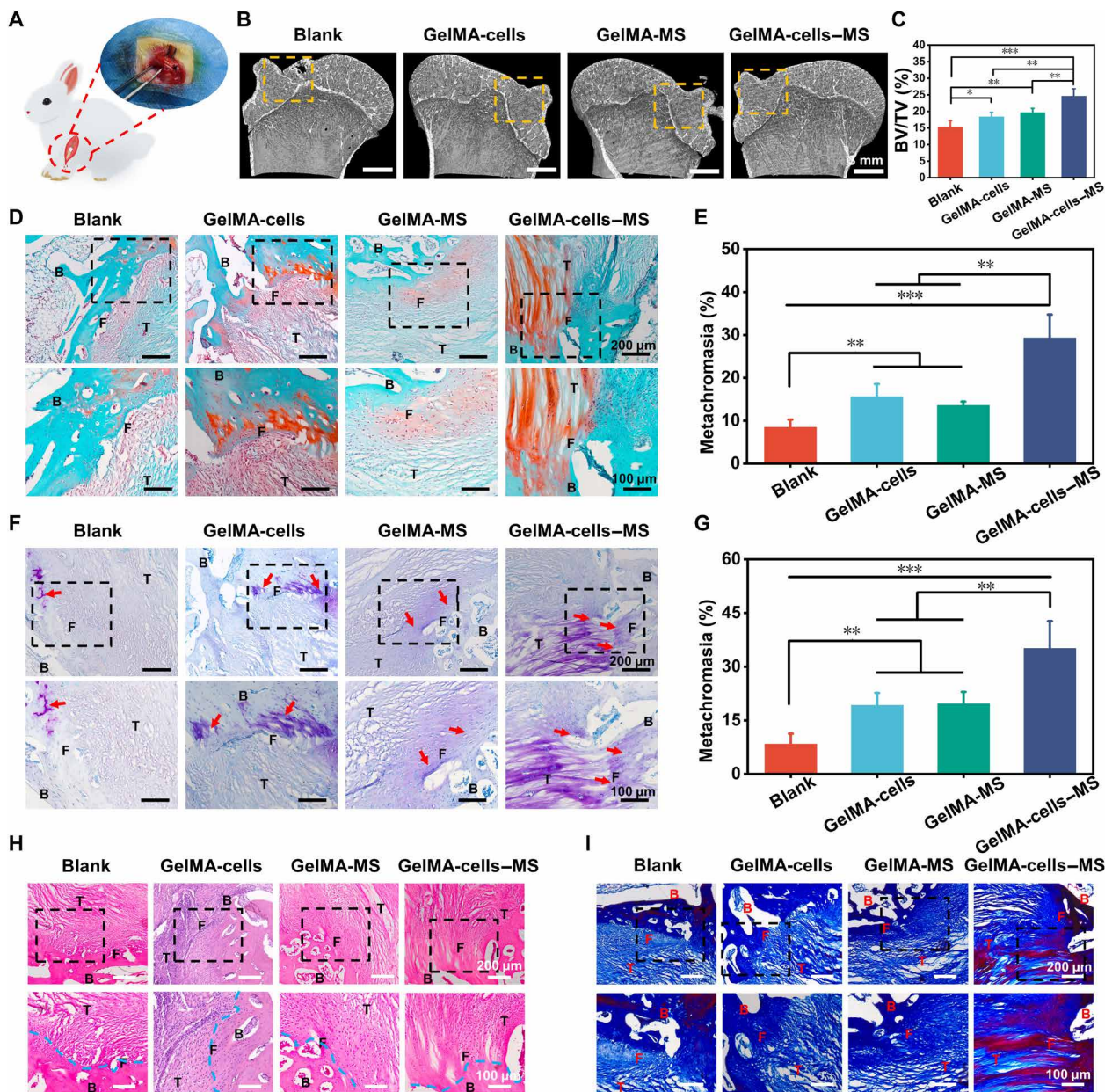
Fig. 5. The multicellular scaffolds based on MS nanoparticles promoted histological structure regeneration of rabbit RCT. (**A**) The schematic diagram of rabbit RCT. (**B**) Representative micro-CT analysis images of bone at tendon-to-bone interface. (**C**) The bone volume fraction (BV/TV) values of bone defect at tendon-to-bone interface in different groups ($n = 4$). (**D**) Representative Safranin O–Fast Green staining images of the tendon-to-bone interface at 12 weeks postoperatively (B, bone; F, fibrocartilage; T, tendon) and (**E**) corresponding semiquantitative analysis of metachromasia ration ($n = 4$). (**F**) Representative toluidine blue staining images of the tendon-to-bone interface at 12 weeks postoperatively and (**G**) corresponding semiquantitative analysis of metachromasia ration ($n = 4$). (**H**) Representative hematoxylin and eosin staining images and (**I**) Masson staining images of the tendon-to-bone interface at 12 weeks postoperatively. *$P < 0.05$, **$P < 0.01$, and ***$P < 0.001$. The multicellular scaffolds based on MS nanoparticles not only promoted the regeneration of bone and fibrocartilage but also facilitated the reconstruction of orderly histological structures.

Blank group, whereas the cortical bones in the other groups were more continuous. Furthermore, the quantitative analysis revealed that the bone volume/total volume (BV/TV) value of the GelMA-cells–MS group was the highest among all groups (Fig. 5C), which confirmed the satisfactory bone repair ability of the multicellular scaffolds containing MS nanoparticles. Then, histological staining was performed to further explore the regeneration ability of scaffolds for the

tendon-to-bone interface. The regeneration of fibrocartilage at interfaces is an essential criterion for judging RCT regeneration (*57*, *58*). Therefore, Safranin O–Fast Green (SO-FG) staining and toluidine blue (TB) staining were conducted to investigate the regeneration of fibrocartilage. As shown in Fig. 5 (D and E), the red area (fibrocartilage) of the GelMA-cells, GelMA-MS, and GelMA-cells–MS groups was obviously bigger than that of the Blank group. The

semiquantitative analysis suggested that the metachromasia ratio of GelMA-cells–MS was significantly higher than that of other groups. Moreover, a similar fibrocartilage regeneration trend was also investigated by TB staining (Fig. 5, F and G), indicating that GelMA-cells–MS promoted the fibrocartilage regeneration in vivo. In addition, according to the results of hematoxylin and eosin (H&E) and Masson staining, there were more ordered tissue structures and more collagen deposition in the GelMA-cells–MS group (Fig. 5, H and I).

The multicellular scaffolds containing MS nanoparticles were demonstrated to have better regeneration outcomes of tendon-to-bone injury compared to those without MS nanoparticles. Therefore, in combination with in vitro experiment results, it could be hypothesized that this excellent repair effect may be attributed to the immunomodulatory function and bidirectional bioactivities of multicellular scaffolds based on MS nanoparticles. On the one hand, a growing number of reports have identified excessive inflammation response as a cause for the regeneration of disorganized scar structures at the tendon-to-bone interface (5, 28, 59). The researchers found that there were more M2 macrophages and less M1 macrophages at the well-healed tendon-to-bone interface (22). Moreover, suppressing the expression of pro-inflammatory cytokines could prevent the formation of peritendinous fibrosis and induce bone and cartilage regeneration, thereby promoting the restoration of interface structures (60). In this study, the multicellular scaffolds containing MS nanoparticles induced more M2 phenotype of macrophages around the injury tissue, thus creating an anti-inflammatory immune microenvironment in vivo, which was beneficial for the restoration of natural structure at the interfaces. On the other hand, some studies have demonstrated that suppressing bone loss and disordered tendon generation after tendon-to-bone injury has a positive effect on interfacial regeneration (4, 61–63). In this study, taking advantage of biomimetic multicellular distribution and bioactive ions released from MS nanoparticles, GelMA-cells–MS could show bidirectional bioactivities (osteogenic and tenogenic differentiation), exhibiting great potential to stimulate osteointegration and tendon maturation simultaneously, which may accelerate integrated regeneration at the tendon-to-bone interface. In short, benefiting from the immunomodulatory function and bidirectional bioactivities, the immunomodulatory multicellular scaffolds accelerated histological structural and functional recovery.

Overall, the multicellular scaffolds containing MS nanoparticles induced fibrocartilage regeneration, improved interfacial structure, and increased collagen deposition, achieving the integrated repair of tendon-to-bone injury.

The effect of macrophage depletion on specific differentiation of the multicellular scaffolds in vivo

It is known that the cross-talk between immune cells, especially macrophages, and tissue scaffolds is important, which is beneficial for regulating cellular differentiation behavior and scaffold-mediated tissue regeneration performance (64, 65). To elucidate the role of macrophages in the specific differentiation of the multicellular scaffolds containing MS nanoparticles in vivo, the macrophage-depleted model of rats was established by injection of clodronate liposomes according to previous reports (66). One group was treated with clodronate liposomes (Scaffold+Clodronate), and another group treated with liposome-encapsulated phosphate-buffered saline (PBS) was used as control (Scaffold+PBS) (Fig. 6A). First, immunofluorescent staining of CD68 was applied to detect the number of macrophages around the scaffolds. As shown in Fig. 6 (B and C), a large number

of macrophages was observed in the Scaffold+PBS group but almost no macrophages were found in the Scaffold+Clodronate group, which demonstrated that the macrophage-depleted model was successfully created. Then, the osteogenic/tenogenic differentiation–related cytokines secreted by the multicellular scaffolds were assayed to investigate the osteogenic/tenogenic differentiation of BMSCs/TSPCs under macrophage-free conditions. Figure 6D demonstrated that all the osteogenic differentiation–related cytokines (*OPN*, *Runx2*, *OCN*, and *BMP2*) in Scaffold+PBS were higher than those in Scaffold+Clodronate. In addition, TSPCs within the multicellular scaffolds of the Scaffold+PBS group also expressed more *ASPN*, *TNMD*, and *TNC* than that of the Scaffolds+Clodronate group (Fig. 6E). These results found that the induced specific differentiation of MS nanoparticles to cells in the multicellular scaffolds was obviously reduced under the macrophage-free condition, showing that the regulation of TSPCs and BMSCs in scaffolds through the immunomodulation of macrophages may be an important pathway by which MS nanoparticles affected tendon-to-bone regeneration. Moreover, *PGE2* is a lipid signaling molecule for pain and inflammation, and macrophages can secrete *PGE2* to affect the process of tissue regeneration (67, 68). Thus, the *PGE2* expression of macrophages was tested to explore the mechanism of MS nanoparticles regulating macrophages for enhancing the specific differentiation of multiple cells in vivo. Figure 6F indicated that the content of *PGE2* in Scaffold+PBS was higher than that in Scaffold+Clodronate. In recent years, there has been increasing evidence that macrophages could modulate some tissue cells, such as bone-associated cells and tendon-associated cells, through the secretion of *PGE2*, thus participating in the process of natural tissue regeneration (67, 69). For osteogenic differentiation, *PGE2* could stimulate *PGE2* receptor 4 (*EP4*) in sensory nerves, thus regulating bone formation by inhibiting sympathetic nerve activity through the central nervous system (70). Besides, it was proven that macrophages could boost skeleton interoception and sprout nerve fibers that sense inflammatory cues via the *PGE2* receptor, which in turn transmitted sensory signals to the central nervous system–activated skeleton interoception, and ultimately induced new bone formation (71). Meanwhile, *PGE2* signaling could also stimulate the proliferation, migration, and adhesion of tenocytes in vitro and promote tendon repair in vivo (72). Together, the multicellular scaffolds containing MS nanoparticles hold the immunomodulatory ability. This immunomodulatory multicellular scaffold may stimulate the *PGE2* secretion of macrophages to enhance the specific differentiation of TSPCs and BMSCs in vivo, either through the central nervous system or directly.

The immunomodulatory effect and mechanism of multicellular scaffolds

To further explore the effect of MS nanoparticles on the immune response of macrophages to regulate the specific differentiation, the RAW 264.7 cells were cocultured with the multicellular scaffolds by a transwell system. As shown in Fig. 7A, the multicellular scaffolds were cultured in the upper chamber and the macrophages were cultured in the lower chamber for 7 days. All scaffolds were divided into four groups, named GelMA-Co (multicellular scaffolds without macrophages and MS nanoparticles), GelMA-Co-5MS (multicellular scaffolds without macrophages), GelMA-Co+RAW (multicellular scaffolds without MS nanoparticles), and GelMA-Co-5MS+RAW (multicellular scaffolds with MS nanoparticles and macrophages). Considering that the GelMA scaffold containing only MS nanoparticles could not reveal the effect of MS nanoparticles in a 3D
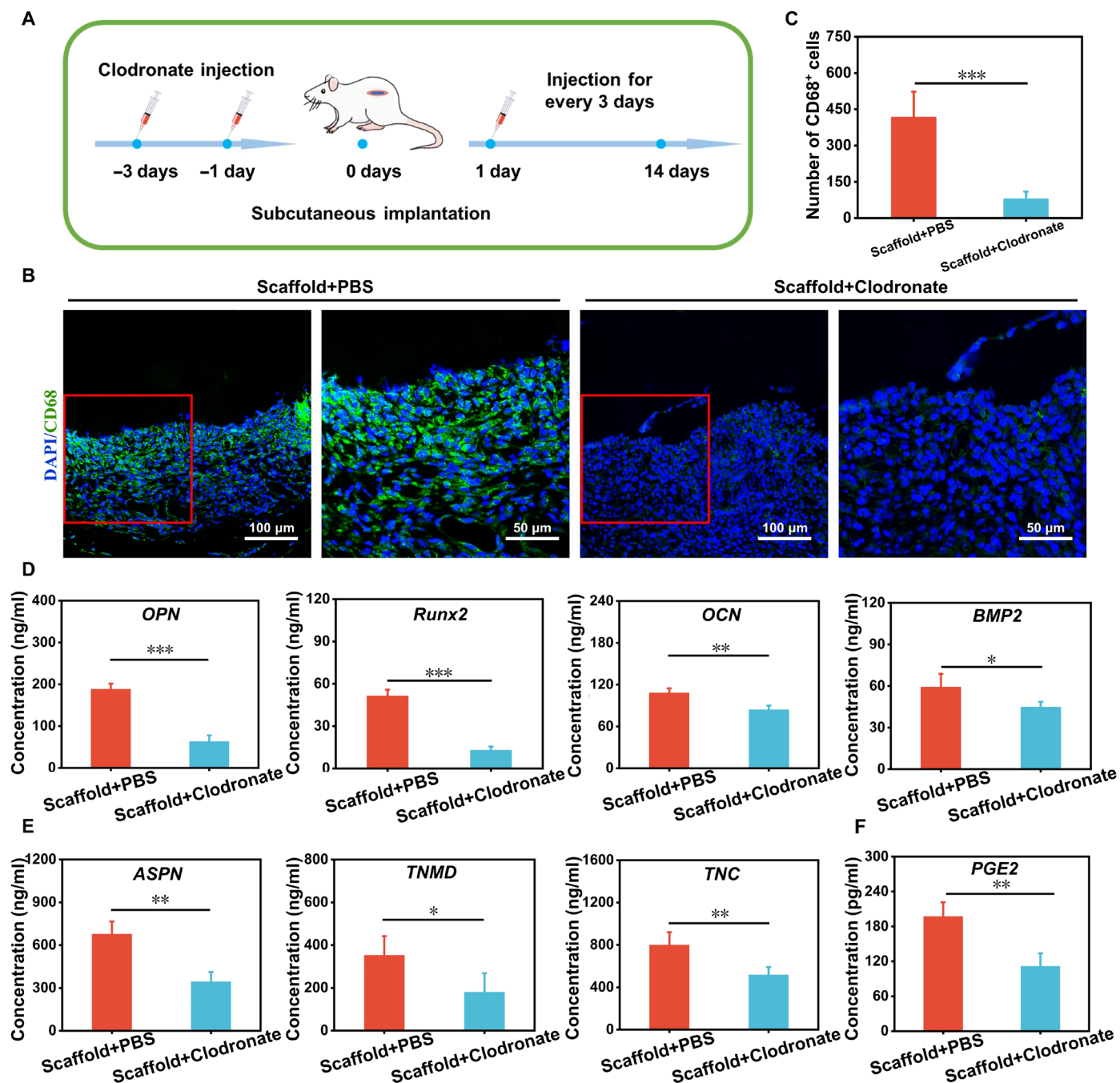
Fig. 6. Subcutaneous implantation of the multicellular scaffolds based on MS nanoparticles in macrophage-depleted rats for assessment of bidirectional activity. (**A**) Time frame of clodronate injection to establish a macrophage depletion model; rats treated with phosphate-buffered saline (PBS) were used as control. (**B**) Immunofluorescence staining images of CD68 protein after implanted scaffolds for 5 days and (**C**) corresponding number statistics of CD68$^+$ cells ($n = 4$). The ELISA of (**D**) osteogenic cytokines (*OPN*, *Runx2*, *OCN*, and *BMP2*) and (**E**) tenogenic cytokines (*ASPN*, *TNMD*, and *TNC*) in multicellular scaffolds based on MS nanoparticles after implanted for 14 days ($n = 4$). (**F**) The *PGE2* secretion of tissues around implanted scaffolds ($n = 4$). *$P < 0.05$, **$P < 0.01$, and ***$P < 0.001$. The multicellular scaffolds based on MS nanoparticles may stimulate the *PGE2* secretion of macrophages to enhance the specific differentiation of TSPCs and BMSCs in vivo.
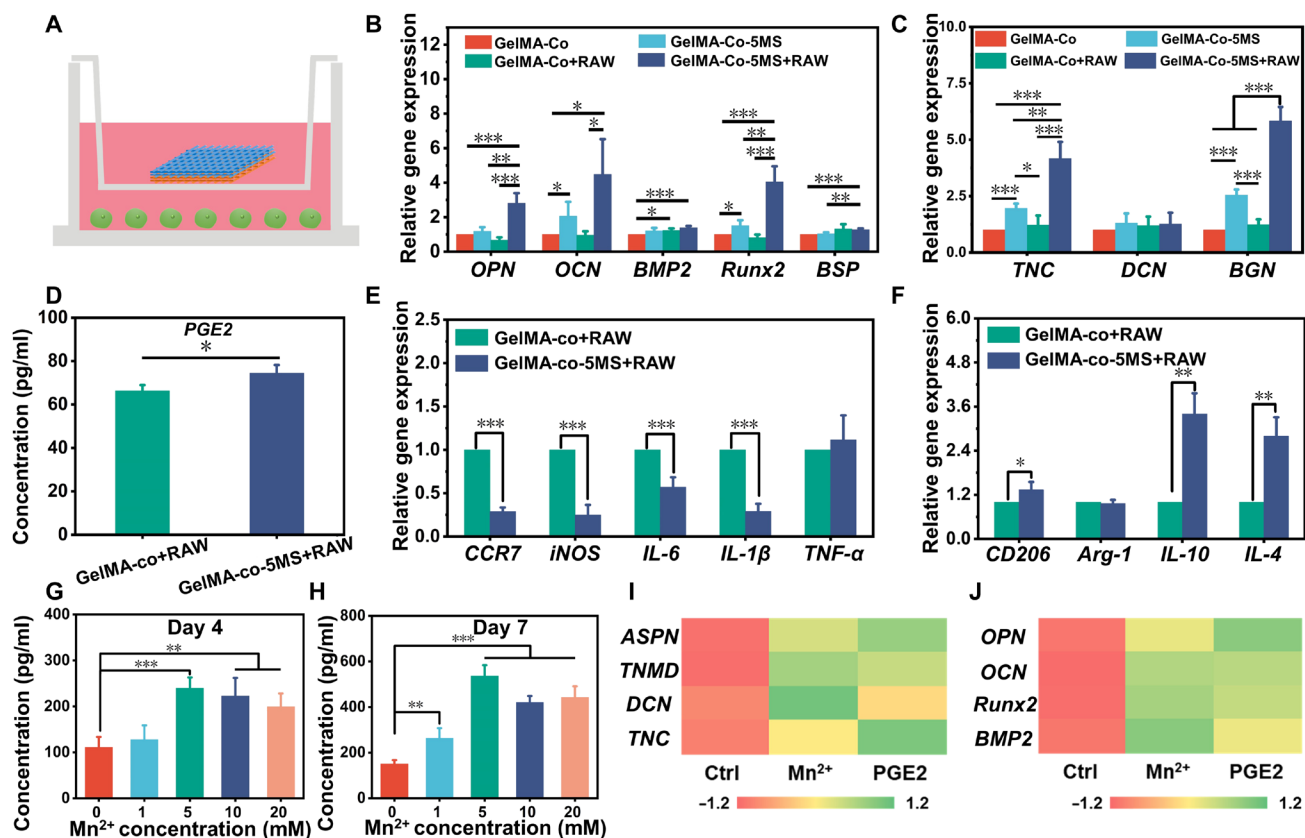
Fig. 7. The immunomodulatory mechanism of multicellular scaffolds based on MS nanoparticles. (**A**) Schematic diagram of the transwell system coculturing multicellular scaffolds and RAW 264.7 cells. (**B**) The osteogenic differentiation–related genes (*OPN*, *OCN*, *BMP2*, *Runx2*, and *BSP*) expression of BMSCs and (**C**) tenogenic differentiation–related genes (*TNC*, *DCN*, and *BGN*) expression of TSPCs in multicellular scaffolds after cocultured with RAW 264.7 cells for 7 days (*n* = 4). (**D**) The *PGE2* concentration of culture medium in the coculture system of the multicellular scaffolds and RAW 264.7 cells at day 7 (*n* = 3). (**E**) The proinflammatory genes (*CCR7*, *iNOS*, *IL-6*, *IL-1β*, and *TNF-α*) expression and (**F**) anti-inflammatory genes (*CD206*, *Arg-1*, *IL-10*, and *IL-4*) expression of RAW 264.7 cells after cocultured with multicellular scaffolds for 7 days (*n* = 4). The *PGE2* expression of macrophages after incubated with a culture medium containing gradient concentration of Mn ions for (**G**) 4 and (**H**) 7 days (*n* = 5). The secretion of (**I**) tenogenic cytokines in TSPCs and (**J**) osteogenic cytokines in BMSCs after being cultured with Mn^{2+}/macrophage-conditioned medium or *PGE2*-containing medium (*n* = 3). *$P < 0.05$, **$P < 0.01$, ***$P < 0.001$. Because of the release of bioactive ions, especially Mn ions, the immunomodulatory multicellular scaffolds containing MS nanoparticles induced the M2 polarization of macrophages and stimulated the expression of *PGE2* in macrophages to simultaneously promote the specific differentiation of TSPCs and BMSCs.

multicellular environment, the GelMA scaffold containing MS nanoparticles was not used as a control. First, real-time quantitative polymerase chain reaction (RT-qPCR) was applied to investigate the effect of macrophages on the specific differentiation of TSPCs and BMSCs in the multicellular scaffolds. Figure 7B exhibited that there was no significant difference in the expression of osteogenic differentiation–related genes (*OPN*, *OCN*, *Runx2*, and *BSP*) between GelMA-Co and GelMA-Co+RAW. Although GelMA-Co-5MS slightly enhanced the expression of *OCN* and *Runx2* as compared to GelMA-Co, GelMA-Co-5MS+RAW substantially up-regulated the expression of *OPN*, *Runx2*, and *BSP* relative to GelMA-Co and GelMA-Co-5MS. Meanwhile, compared with GelMA-Co+RAW, GelMA-Co-5MS+RAW up-regulated the expression of *OPN*, *OCN*, and *Runx2* in BMSCs. In addition, the expressions of *TNC*, *DCN*, and *BGN* in TSPCs in the GelMA-Co+RAW group were not significantly different from those in the GelMA-Co group (Fig. 7C). The *TNC* and *BGN* expressions of TSPCs in GelMA-Co-5MS+RAW were higher than TSPCs in other scaffolds. On the basis of the above results, it was found that coculturing with macrophages enhanced the osteogenic

differentiation of BMSCs and tenogenic differentiation of TSPCs in multicellular scaffolds containing MS nanoparticles, whereas no such effect was observed in pure multicellular scaffolds cocultured with macrophages. These results revealed that MS nanoparticles could stimulate the specific differentiation of BMSCs and TSPCs by modulating macrophages.

Subsequently, the expression of M1 phenotype–related genes (*CCR7*, *iNOS*, *IL-6*, *IL-1β*, and *TNF-α*), M2 phenotype–related genes (*CD206*, *Arg-1*, *IL-10*, and *IL-4*), and *PGE2* of RAW 264.7 cells was examined to investigate the immunomodulatory effect of MS nanoparticles on macrophages (Fig. 7, D to F). Encouragingly, the GelMA-Co-5MS+RAW group expressed more *CD206*, *IL-10*, *IL-4*, and *PGE2* but produced significantly less *CCR7*, *iNOS*, *IL-6*, and *IL-1β*, demonstrating that the multicellular scaffolds containing MS nanoparticles induced M2 macrophage polarization, which may be due to the bioactive ions released from MS nanoparticles. Considerable pieces of evidence have confirmed that the bioactive ions generated by inorganic biomaterials can induce macrophage polarization to achieve the construction of the immune microenvironment (*73*, *74*).

Among them, bioceramics that could release Si ions were reported to suppress macrophage inflammatory responses through inhibiting mitogen-activated protein kinase (MAPK) and nuclear factor κB (NF-κB) signaling pathways and enhancing cysteine-dependent apoptotic activity of macrophages (75). Besides, Mn ions could reduce the expression of pro-inflammatory cytokines and increase the secretion of anti-inflammatory cytokines to induce the M2 phenotype of macrophages (36). These above experiments suggested that the multicellular scaffolds containing MS nanoparticles could regulate the immunomodulatory effect of macrophages through the release of Mn and Si ions, thereby enhancing bidirectional bioactivities. It has been proven that Si ions reduce the secretion of inflammatory cytokines by suppressing the MAPK and NF-κB pathways (29, 75). Although Mn ions have been demonstrated the inhibition of pro-inflammatory gene expression and the promotion of anti-inflammatory gene expression, the signaling pathway through which Mn ions induce macrophages to secrete more anti-inflammatory cytokines and reduce the expression of pro-inflammatory genes is still unknown. Thus, on the basis of the above in vitro and subcutaneous experiment results, we further explored the effect of Mn ions on the secretion of *PGE2* in macrophages. The culture media containing gradient content of Mn ions were prepared to explore the influence of Mn ions on the macrophages. After 4 and 7 days of incubation with a series of Mn ion–containing culture media, it was found that Mn ions stimulated macrophages to secrete more *PGE* (Fig. 7, G and H). Subsequently, comparing the effect of osteogenic/tenogenic differentiation of BMSCs/TSPCs induced by Mn ions/macrophage-conditioned medium and *PGE2*-containing medium, they exhibited proximity facilitation of osteogenic differentiation of BMSCs and tenogenic differentiation of TSPCs (Fig. 7, I and J). Therefore, Mn ions had a notable enhancement effect on the secretion of *PGE2* in macrophages. Moreover, the regulatory trend of the immune microenvironment stimulated by Mn ions on the specific differentiation of TSPCs and BMSCs was similar to that of *PGE2*. Recently, Qiao *et al.* (71) found that divalent metal cations could stimulate the expression of *prostaglandin E synthase* (*PTGES*) and the generation of *cyclooxygenase-2* (*COX2*) protein, thus promoting the synthesis and secretion of *PGE2* in macrophages. Hence, it was reasonable to infer that Mn ions could induce the secretion of *PGE2* in macrophages to enhance the tenogenic differentiation of TSPCs and osteogenic differentiation of BMSCs. In short, these results revealed the important role of *PGE2* in the process of immunomodulatory tendon-to-bone regeneration. The immunomodulatory scaffolds containing MS nanoparticles released bioactive ions, primarily Mn ions, to stimulate macrophages to secrete *PGE2*, which then acted on tissue cells to regulate the specific differentiation and further promote tissue regeneration.

In this study, although the immunomodulatory multicellular scaffolds could achieve successfully the immunomodulation and integrated regeneration of tendon-to-bone injury, there were still some limitations of the present work. First, despite Mn ions could affect bidirectional bioactivities by stimulating the secretion of *PGE2* in macrophages, the specific signaling pathways or modes of this phenomenon remained unclear. Moreover, the effect of immunomodulatory multicellular scaffolds promoting tendon-to-bone injury repair via macrophages was explored through different animal experiments (RCT and macrophage-depleted models) in this study, which may not be direct enough. In future research, it will be valuable to investigate the specific ways through which *PGE2* stimulated by Mn ions affects the bidirectional differentiation of tendon and bone. In addition, the

establishment of a macrophage-depleted RCT model deserves to be considered for a more intuitive analysis in the future.

In conclusion, we successfully developed an immunomodulatory multicellular scaffold based on MS nanoparticles through 3D bioprinting for tendon-to-bone injury repair. First, taking advantage of the synergistic effect of MS nanoparticles and encapsulating multiple cells, the multicellular scaffolds performed excellent ability of osteogenic differentiation and tenogenic differentiation. Moreover, MS nanoparticles within the scaffold constructed a favorable immune microenvironment under the coculture system of multicellular scaffolds and macrophages, which enhanced the bidirectional differentiation of the multicellular scaffolds. Encouragingly, after implantation into three animal models, the multicellular scaffolds containing MS nanoparticles achieved immunomodulation in vivo and notably enhanced integrated regeneration, mechanical properties recovery, and better motor function at the tendon-to-bone interface. In addition, the underlying mechanism of immunomodulatory scaffolds was well revealed. It was found that Mn ions stimulated the secretion of *PGE2* in macrophages to promote the specific differentiation of multicellular scaffolds and induced tendon-to-bone regeneration. All in all, the multicellular scaffolds with immunomodulatory and integrated regenerative functions have great potential in soft-to-hard tissue interface regeneration.

MATERIALS AND METHODS
Fabrication of hollow MS nanospheres
The raw materials for synthesizing MS nanoparticles were listed as follows: calcium chloride anhydrous ($CaCl_2$), ammonium fluoride (NH_4F), tetraethoxysilane (TEOS), cetyltrimethylammonium bromide (CTAB), and sodium acetate anhydrous (CH_3COONa) were purchased from Sinopharm Chemical Reagent Co. Ltd. (Shanghai, China). Manganese chloride tetrahydrate ($MnCl_2 \cdot 4H_2O$) was purchased from Sigma-Aldrich Co. Ltd. (USA). MS nanoparticles were synthesized according to a previous study (36). Briefly, 3 g of NH_4F and 1.8 g of CTAB were added in 500 ml of deionized water separately. Then, the mixed solution was continuously stirred at 80°C until it became homogenous. Subsequently, 9 ml of TEOS was slowly added into the above solution and aged for 12 hours. After being centrifuged at 8000 rpm for 15 min, silica nanospheres were obtained from the precipitate and washed with ethanol and deionized water. Next, 0.1 g of silica nanospheres, 0.05 g of CH_3COONa, and 0.1 g of $MnCl_2 \cdot 4H_2O$ were added in 40 ml of deionized water, respectively, and triethanolamine was added into the above mixture until the pH was 7.5. Then, the mixed solution reacted at 110°C for 24 hours in an enclosed autoclave. After the solution cooled, the obtained precipitate was washed with water and anhydrous ethanol. Last, the obtained products were calcined at 650°C for 6 hours.

Cell culture
BMSCs were isolated from male rabbit or rat femur tissue and TSPCs were extracted from male rabbit or rat tendon tissues. Both of them were cultured in minimum essential medium alpha (Gibco, USA) medium containing 10% fetal bovine serum (FBS; Gibco, USA) and 1% penicillin-streptomycin (P/S; Gibco, USA). Murine-derived macrophage cell line RAW 264.7 cells were obtained from the cell bank of the Chinese Academy of Sciences. RAW 264.7 cells were cultured in Dulbecco's modified Eagle's medium supplemented with 10% FBS and 1% P/S. All cells were cultured under 37°C and a 5% CO_2

incubator. The isolated cells evaluated the morphology, surface markers related to mesenchymal/hematopoietic stem cells, and unique protein expression through an optical microscope (Leica, Germany), flow cytometry (BD Biosciences, America), and immunofluorescent staining assay (fig. S1). The tested markers in this study included CD90, CD44, and CD34 (Oricell, RAXMX-09011, China).

Preparation of bioinks and cell bioprinting
Gelatin methacryloyl (GelMA) was synthesized as in the previous study (32, 48). To obtain a 6% GelMA (w/v) solution, 0.6 g of GelMA and 0.025 g of lithium phenyl-2,4,6-trimethylbenzoylphosphinate (LAP) were dissolved into PBS at 60°C. The GelMA solution was filtered through 0.22-μm filters for sterilization. After being sterilized by ultraviolet light, MS nanoparticles were incorporated into GelMA solution (the mass ratio of MS nanoparticles to GelMA foams was 0, 2, 5, 10, and 15%). Next, cell suspension containing TSPCs or BMSCs (5×10^6 cells/ml) was mixed with the above GelMA solution to obtain bioinks containing different concentrations of MS nanoparticles. Afterward, the bioinks were transferred into metal syringes. A 3D bioprinting platform equipped with a temperature control system (Bioscaffolder 3.2, GeSiM, Germany) was used to fabricate scaffolds. After being refrigerated at 4°C for 20 min, the cell-laden bioinks were printed on the condition of 20°C temperature and 30-kPa pressure to obtain scaffolds. Subsequently, the scaffolds were immediately cross-linked via blue light exposure for 30 s. Last, the bioprinted cell-laden scaffolds were placed into 24-well plates with 1 ml of culture medium and transferred to a humidified incubator with 5% CO_2 at 37°C.

The ionic release behavior of MS nanoparticles in scaffolds
To test the concentration of Mn and Si ions released from MS nanoparticles in scaffolds, the scaffolds in each group were cultured with 1 ml of culture medium at 37°C. Subsequently, the culture medium was collected at specific time points (days 1, 3, 5, 7, 14, and 21). After filtration, the concentration of Mn and Si ions in the culture medium was detected by ICP-OES (710-ES, Varian, USA).

Proliferation activities of cells in bioprinted scaffolds
The CCK-8 kit (Dojindo, Japan) was used to assess the proliferation activities of TSPCs and BMSCs within the multicellular scaffolds. Briefly, after being cultured in a 24-well plate for different days (1, 7, 14, and 21 days), the scaffolds were digested with collagenase buffer (EFL-GM-LS-001, Suzhou, China). Subsequently, the collected cells were treated with 10% (v/v) CCK-8 solution for 2 hours. Then, the absorbance values were measured by a multifunction microplate reader (Epoch, BIO-TEK, USA) at 450 nm.

Live/dead assay
Calcein-AM/PI Double Staining Kit (Dojindo, Japan) was used to characterize the viability of TSPCs and BMSCs in the scaffolds. At each special time point, the scaffolds were washed with PBS solution and incubated with the working solution (AM:PI:PBS = 2:1:1000) for 20 min. Then, the scaffolds were immediately observed by CLSM (TCS SP8, Leica, Germany). Living cells were detected by 488 nm excitation light for green while dead cells were detected by 556 nm excitation light for red.

ALP staining assay
To evaluate the mineralization capacity of BMSCs in scaffolds, the expression of ALP was analyzed by the ALP staining. First, after being cultured for 7 days and 14 days, the cells within the scaffolds were digested by collagenase buffer (EFL-GM-LS-001, Suzhou, China) for 2 h at 37°C so that they could be reattached to a well plate. Then, the cells were washed with PBS solution and fixed with 4% paraformaldehyde for 30 min, then washed with distilled water and stained with ALP staining kits (Beyotime, China) for 2 h at 37°C. Next, the level of ALP staining values was quantified using ALP assay kits (Beyotime, China) according to the manufacturer's instructions. Briefly, the cells were lysed using cell lysate, and the supernatant was collected. Afterward, p-nitrophenyl phosphate solution was added into the supernatant with 30 min of reaction at 37°C, and the absorbance value of the yellow product at 405 nm was measured. Furthermore, a BCA protein detection kit was applied to determine the amount of total protein in the supernatant. The activity of ALP was then calculated using a standard curve.

ARS staining assay
ARS staining assay was conducted to detect the calcium nodule within the multicellular scaffolds. After 7 days and 14 days of culture, respectively, the scaffolds were washed with PBS solution and fixed with 4% paraformaldehyde for 30 min. Next, the scaffolds were washed with distilled water and stained with ARS solution (2%, pH = 4.2) for 20 min. Afterward, the scaffolds were washed with distilled water, dried, and imaged by a digital camera and a microscope. Furthermore, the scaffolds were immersed in 10% acetic acid and neutralized with 10% ammonium hydroxide to semiquantitatively analyze the ARS staining value, and the absorbance value of supernatant at 450 nm was measured via a multifunction microplate reader (Epoch, BIO-TEK, USA).

Spatial distribution of cells in multicellular scaffolds
Before the construction of 3D bioprinted multicellular scaffolds, the cells were labeled with different fluorescent markers (CellTracker, Invitrogen, USA), respectively. BMSCs were marked with red fluorescence while TSPCs were marked with green fluorescence. Then, the multicellular scaffolds were prepared and cultured under dark conditions. At different time points (1, 4, 7, and 14 days), the scaffolds were fixed with 4% paraformaldehyde and observed via CLSM (TCS SP8, Leica, Germany).

Immunofluorescent staining assay
An immunofluorescence staining assay was performed to detect the expression of specific proteins in cells. Osteopontin (OPN) is a secreted glycoprotein that is important in regulating biomineralization in bone tissue (76). Tenomodulin (TNMD) is a type II transmembrane glycoprotein and a phenotypic marker during tendon development, which is highly expressed in connective tissues (50, 51). After a 14-day culture, the scaffolds were incubated with 4% paraformaldehyde for 30 min, then treated with 0.5% Triton X-100 solution and washed three times with PBS solution. Next, a 5% bovine serum albumin solution was used to block the cells in the scaffolds for 30 min at ambient temperature. Subsequently, the scaffolds were immersed in primary antibody solution overnight at 4°C. After the primary antibody was removed, the cells were incubated with the corresponding secondary antibody solution at 37°C for 1 hour under the dark condition. At last, the immunofluorescence staining images were captured by CLSM (TCS SP8, Leica, Germany). The semiquantitative analysis of the images was conducted by ImageJ software. The specific information on the antibodies used was shown as follows: anti-OPN (1:200

dilution; PA5-34579, Thermo Fisher Scientific) and anti-TNMD (1:200 dilution; PA5-112767, Thermo Fisher Scientific).

Gene expression

The bioprinted scaffolds containing cells and RAW 264.7 cells were cocultured using the transwell method. The gene expression of the cells within bioprinted scaffolds and RAW 264.7 cells was detected by RT-qPCR. Briefly, after being cocultured for 7 days, the scaffolds were incubated with GelMA lysis buffer (EFL-GM-LS-001, Suzhou, China) for 2 hours at 37°C to collect all cells. Then, the total RNA was extracted by TRIzol reagent (TAKARA, Japan). Subsequently, cDNA was synthesized through the PrimeScript 1st Strand cDNA synthesis kit (TOYOBO, Japan). Next, the RT-qPCR was conducted by StepOnePlus real-time systems (Applied Biosystems, USA). At last, the values were calculated by the $2^{-\Delta\Delta CT}$ method. The primer sequences are listed in table S1.

Animal model and surgical procedure

All animal experiments in this study were approved and reviewed by the Institutional Animal Care and Use Committee of Nanjing First Hospital, Nanjing Medical University (No. DWSY-22030156). The rat RCT model was established to evaluate the immunomodulation and restoration of damaged tissue function in vivo. The Sprague-Dawley rats (male, 6 weeks old) were randomly divided into four groups: healthy rats without operation group (Normal), no scaffold group (Blank), MS nanoparticle–free scaffold group (GelMA-Cells), and scaffold containing MS nanoparticle and cell group (GelMA-cells–MS). The purpose of this experiment was to explore the in vivo role of MS nanoparticles in the 3D multicellular system. However, the GelMA-MS group could not demonstrate the immunomodulatory effect of MS nanoparticles in a 3D multicellular system. Hence, in accordance with the "3R" principle (reduction, replacement, and refinement) of animal experiments, the GelMA-MS nanoparticle scaffold was not taken into consideration. After anesthesia, hair removal, and sterilization, the skin and muscle at the shoulder of rats were cut to expose the rotator cuff tissue. Then, the supraspinatus tendon was completely detached from the bone, and 0.8-mm-diameter tunnels were drilled into the bone. Next, the scaffolds were secured to the tendon-to-bone interface, and the tendon was sutured to the bone through the tunnels with 5-0 Ethicon sutures. Last, the muscles and skin were closed sequentially. After 4, 7, and 14 days, the rats in each group were executed and the tissues surrounding the scaffolds were evaluated by immunofluorescent staining assay. At predefined postoperative time points (1, 4, and 8 weeks), the gait analysis was conducted. At 8 weeks postoperatively, the remnant rats were euthanized and the repair tissues were collected.

To evaluate the in vivo repair effect of the scaffolds, the rabbit RCT model was established. First, 16 male mature New Zealand white rabbits weighing 3.0 ± 0.5 kg were randomized into four groups: no scaffold group (Blank), MS nanoparticle–free scaffold group (GelMA-cells), cell-free scaffold group (GelMA-MS), and scaffold containing MS nanoparticle and cell group (GelMA-cells-MS). Next, after being anesthetized, the rabbits in all groups were kept in a supine position, shaved, and disinfected at the shoulders. By incising the shoulder skin, the rotator cuff tissue, especially the supraspinatus tendon, was exposed. Then, the tendon was isolated from the bone, and a hole with a diameter of 4 mm was drilled at the tuberosity. Next, the scaffolds were cut into cylinders with 4-mm diameter and placed into the hole. Last, the tendon was sutured to the bone with 3-0 Ethibond

sutures, and the wound was closed and disinfected again. At 12 weeks postoperatively, the rabbits were euthanized to collect the muscle-tendon-bone complexes.

To investigate the effect of macrophage depletion on enhanced regenerative outcomes induced by the scaffolds containing MS nanoparticles, the macrophage depletion model of Sprague-Dawley rats was created according to a previous report (57). Clodronate liposomes (LIPOSOMA, Netherlands) were applied to deplete macrophages. First, the Sprague-Dawley rats (male, 6 weeks old) were randomly divided into two groups: one group was treated with liposome-encapsulated PBS (GelMA-cells-MS+PBS) and another group was treated with clodronate liposomes (GelMA-cells-MS+clodronate). All of the rats received injections on days 1 and 3 before the implantation of scaffolds. After being shaved, the backs of the rats were sterilized with iodine solution. Then, a subcutaneous cavity was created on the side of the back, enabling the insertion of a scaffold. The skin incision was closed by 4-0 Ethibond sutures. Subsequently, sterile liposomal clodronate or liposome-encapsulated PBS (50 mg/kg) was locally injected in the cavity every 3 days from the first postoperative day. After 2 weeks of operation, the rats were euthanized and the scaffolds were collected. When analyzing the above results, the researchers were blinded to the grouping of animals.

Histological analysis

All collected tissues were fixed in 4% paraformaldehyde solution and then decalcified in 10% EDTA decalcification solution (Sangon Biotech, Shanghai, China) for 1 month. Next, the completely decalcified samples were sequentially immersed in PBS/10% sucrose solution for 4 hours and PBS/30% sucrose solution overnight. Subsequently, the tissues were embedded in an OCT medium and sectioned for 10 μm. After being thawed at room temperature, the sections were stained with SO-FG staining kits (Solarbio, Beijing, China), TB staining (Servicebio, Wuhan, China), H&E staining kits (Beyotime Biotechnology, Shanghai), and Masson staining kits (Solarbio, Beijing, China) to analyze the repair effect of tendon and bone tissues. The images were photographed by an optical microscope (Leica, Germany). Semiquantitative analysis of the area ratio of fibrocartilage at the interface was performed using ImageJ software.

Micro-CT analysis

To assess bone regeneration at the tendon-to-bone interface, a micro-CT instrument (SKYSCAN1172, Bruker, Germany) was applied to scan the newly formed bone. Afterward, the CT volume was utilized to reconstruct the 3D images of bone and the CT analyzer program was used to calculate the BV/TV.

Biomechanical evaluation

The biomechanical properties of the samples were determined using a universal mechanical testing machine (Instron-5566, USA). The supraspinatus muscle and its insertion were retained to clamp easily, and all extraneous tissues were discarded. To keep the sample moist and increase the friction between the sample and the clamp, the supraspinatus tendon was wrapped using medical gauze soaked in saline. Then, the samples were fixed through the longitudinal axis of the humerus. The detailed operating procedure was in accordance with the previous article (34). The ultimate failure load (in newtons), elastic modulus (in megapascals), and stiffness (in newtons per millimeter) were recorded and calculated.

ELISA

The harvested samples were immersed in pre-cooled PBS solution, thoroughly ground, and centrifuged at 1×10^5 rpm for 10 min to obtain supernatants. *CCR7*, *CD206*, *OPN*, *OCN*, *BMP2*, *Runx2*, *ASPN*, *TNMD*, *DCN*, and *TNC* in the obtained supernatants were detected with ELISA kits (Chutai, Shanghai, China) following the manufacturer's instructions.

Gait analysis

The gait analysis was conducted to evaluate the function of the repaired rotator cuff tissues. First, a walking track system was designed with clear and black acrylic panels (length × width × height = $120 \times 20 \times 16$ cm^3) according to a previous report (*56*). Before the test, the left forepaws of rats were painted red and their right forepaws were painted blue with washable ink. Then, the clear acrylic panel was covered with white paper so that the rats could walk through and leave pawprints. After collecting the recorded pawprints, the relevant parameters were analyzed. To quantify and compare the degree of asymmetry between repaired and normal sites, the asymmetry index (AI) was calculated as follows

$$AI(\%) = \frac{(NS - ES) \times (NS + ES)}{0.5} \times 100$$

where NS represented the measured value of the normal side and ES represented the measured value of the repaired side.

Statistical analysis

All data were expressed as means ± SD and analyzed in Origin 2017 software (OriginLab, USA). The dates were conducted by using one-way analysis of variance (ANOVA) testing. A significant difference was considered when *$P < 0.05$, **$P < 0.01$, or ***$P < 0.001$.

Supplementary Materials

This PDF file includes:
Figs. S1 to S7
Table S1
Legend for movie S1
References

Other Supplementary Material for this manuscript includes the following:
Movie S1

REFERENCES AND NOTES

1. S. Font Tellado, E. R. Balmayor, M. Van Griensven, Strategies to engineer tendon/ligament-to-bone interface: Biomaterials, cells and growth factors. *Adv. Drug Deliv. Rev.* **94**, 126–140 (2015).
2. I. Calejo, R. Costa-Almeida, R. L. Reis, M. E. Gomes, Enthesis tissue engineering: Biological requirements meet at the interface. *Tissue Eng. Part B Rev.* **25**, 330–356 (2019).
3. H. H. Lu, S. Thomopoulos, Functional attachment of soft tissues to bone: Development, healing, and tissue engineering, in *Annual Review of Biomedical Engineering*, vol. 15, M. L. Yarmush, Ed. (Annual Reviews, 2013), pp. 201–226.
4. C. L. Zhu, J. C. Qiu, S. Thomopoulos, Y. N. Xia, Augmenting tendon-to-bone repair with functionally graded scaffolds. *Adv. Healthc. Mater.* **10**, e2002269 (2021).
5. G. P. Dang, W. Qin, Q. Q. Wan, J. T. Gu, K. Y. Wang, Z. Mu, B. Gao, K. Jiao, F. R. Tay, L. N. Niu, Regulation and reconstruction of cell phenotype gradients along the tendon-bone interface. *Adv. Funct. Mater.* **33**, 2210275 (2023).
6. X. Jiang, Y. Kong, M. Kuss, J. Weisenburger, H. Haider, R. Harms, W. Shi, B. Liu, W. Xue, J. Dong, J. Xie, P. Streubel, B. Duan, 3D bioprinting of multilayered scaffolds with spatially differentiated ADMSCs for rotator cuff tendon-to-bone interface regeneration. *Appl. Mater. Today* **27**, 101510 (2022).
7. T. Lei, T. Zhang, W. Ju, X. Chen, B. C. Heng, W. Shen, Z. Yin, Biomimetic strategies for tendon/ligament-to-bone interface regeneration. *Bioact. Mater.* **6**, 2491–2510 (2021).
8. D. Zbrojkiewicz, C. Vertullo, J. E. Grayson, Increasing rates of anterior cruciate ligament reconstruction in young Australians, 2000–2015. *Med. J. Australia* **208**, 354–358 (2018).
9. B. Shiroud Heidari, R. Ruan, E. Vahabli, P. Chen, E. M. De-Juan-Pardo, M. Zheng, B. Doyle, Natural, synthetic and commercially-available biopolymers used to regenerate tendons and ligaments. *Bioact. Mater.* **19**, 179–197 (2023).
10. S. A. Rodeo, H. G. Potter, S. Kawamura, A. S. Turner, H. J. Kim, B. L. Atkinson, Biologic augmentation of rotator cuff tendon-healing with use of a mixture of osteoinductive growth factors. *J. Bone Joint Surg. Am.* **89**, 2485–2497 (2007).
11. K. Yasuda, F. Tomita, S. Yamazaki, A. Minami, H. Tohyama, The effect of growth factors on biomechanical properties of the bone-patellar tendon-bone graft after anterior cruciate ligament reconstruction - A canine model study. *Am. J. Sports Med.* **32**, 870–880 (2004).
12. X. Li, R. Cheng, Z. Sun, W. Su, G. Pan, S. Zhao, J. Zhao, W. Cui, Flexible bipolar nanofibrous membranes for improving gradient microstructure in tendon-to-bone healing. *Acta Biomater.* **61**, 204–216 (2017).
13. C. Zhu, S. Pongkitwitoon, J. Qiu, S. Thomopoulos, Y. Xia, Design and fabrication of a hierarchically structured scaffold for tendon-to-bone repair. *Adv. Mater.* **30**, e1707306 (2018).
14. R. H. Yang, G. Li, C. Y. Zhuang, P. Yu, T. J. Ye, Y. Zhang, P. Y. Shang, J. J. Huang, M. Cai, L. Wang, W. G. Cui, L. F. Deng, Gradient bimetallic ion-based hydrogels for tissue microstructure reconstruction of tendon-to-bone insertion. *Sci. Adv.* **7**, eabg3816 (2021).
15. Y. Tang, C. Chen, F. Liu, S. Xie, J. Qu, M. Li, Z. Li, X. Li, Q. Shi, S. Li, X. Li, J. Hu, H. Lu, Structure and ingredient-based biomimetic scaffolds combining with autologous bone marrow-derived mesenchymal stem cell sheets for bone-tendon healing. *Biomaterials* **241**, 119837 (2020).
16. C. Chen, Y. Chen, M. Li, H. Xiao, Q. Shi, T. Zhang, X. Li, C. Zhao, J. Hu, H. Lu, Functional decellularized fibrocartilaginous matrix graft for rotator cuff enthesis regeneration: A novel technique to avoid in-vitro loading of cells. *Biomaterials* **250**, 119996 (2020).
17. L. Bai, Q. Han, Z. Meng, B. Chen, X. Qu, M. Xu, Y. Su, Z. Qiu, Y. Xue, J. He, J. Zhang, Z. Yin, Bioprinted living tissue constructs with layer-specific, growth factor-loaded microspheres for improved enthesis healing of a rotator cuff. *Acta Biomater.* **154**, 275–289 (2022).
18. W. Su, J. Guo, J. Xu, K. Huang, J. Chen, J. Jiang, G. Xie, J. Zhao, S. Zhao, C. Ning, Gradient composite film with calcium phosphate silicate for improved tendon -to-Bone intergration. *Chem. Eng. J.* **404**, 126473 (2021).
19. S. F. Tellado, S. Chiera, W. Bonani, P. S. P. Poh, C. Migliaresi, A. Motta, E. R. Balmayor, M. van Griensven, Heparin functionalization increases retention of TGF-β2 and GDF5 on biphasic silk fibroin scaffolds for tendon/ligament-to-bone tissue engineering. *Acta Biomater.* **72**, 150–166 (2018).
20. J. Hou, R. Yang, I. Vuong, F. Li, J. Kong, H.-Q. Mao, Biomaterials strategies to balance inflammation and tenogenesis for tendon repair. *Acta Biomater.* **130**, 1–16 (2021).
21. J. Lin, W. Zhou, S. Han, V. Bunpetch, K. Zhao, C. Liu, Z. Yin, H. Ouyang, Cell-material interactions in tendon tissue engineering. *Acta Biomater.* **70**, 1–11 (2018).
22. E. Dagher, P. L. Hays, S. Kawamura, J. Godin, X. H. Deng, S. A. Rodeo, Immobilization modulates macrophage accumulation in tendon-bone healing. *Clin. Orthop. Relat. R.* **467**, 281–287 (2009).
23. J. Lu, C. S. Chamberlain, M. L. Ji, E. E. Saether, E. M. Leiferman, W. J. Li, R. Vanderby, Tendon-to-bone healing in a rat extra-articular bone tunnel model: A comparison of fresh autologous bone marrow and bone marrow-derived mesenchymal stem cells. *Am. J. Sports Med.* **47**, 2729–2736 (2019).
24. P. T. Jensen, K. L. Lambertsen, L. H. Frich, Assembly, maturation, and degradation of the supraspinatus enthesis. *J. Shoulder Elbow Surg.* **27**, 739–750 (2018).
25. T. A. Wynn, K. M. Vannella, Macrophages in tissue repair, regeneration, and fibrosis. *Immunity* **44**, 450–462 (2016).
26. S. P. Zhang, S. J. Chuah, R. C. Lai, J. H. P. Hui, S. K. Lim, W. S. Toh, MSC exosomes mediate cartilage repair by enhancing proliferation, attenuating apoptosis and modulating immune reactivity. *Biomaterials* **156**, 16–27 (2018).
27. Z. Julier, A. J. Park, P. S. Briquez, M. M. Martino, Promoting tissue regeneration by modulating the immune system. *Acta Biomater.* **53**, 13–28 (2017).
28. H. H. Gao, L. R. Wang, H. C. Jin, Z. Q. Lin, Z. Y. Li, Y. H. Kang, Y. Lyu, W. Q. Dong, Y. F. Liu, D. Y. Shi, J. Jiang, J. Z. Zhao, Regulating macrophages through immunomodulatory biomaterials is a promising strategy for promoting tendon-bone healing. *J. Funct. Biomater.* **13**, 243 (2022).
29. K. Zheng, W. Niu, B. Lei, A. R. Boccaccini, Immunomodulatory bioactive glasses for tissue regeneration. *Acta Biomater.* **133**, 168–186 (2021).
30. B. Choi, C. Lee, J.-W. Yu, Distinctive role of inflammation in tissue repair and regeneration. *Arch. Pharm. Res.* **46**, 78–89 (2023).
31. C. Qin, J. Ma, L. Chen, H. Ma, H. Zhuang, M. Zhang, Z. Huan, J. Chang, N. Ma, C. Wu, 3D bioprinting of multicellular scaffolds for osteochondral regeneration. *Mater. Today* **49**, 68–84 (2021).
32. H. J. Zhang, C. Qin, M. Zhang, Y. H. Han, J. G. Ma, J. F. Wu, Q. Q. Yao, C. T. Wu, Calcium silicate nanowires-containing multicellular bioinks for 3D bioprinting of neural-bone constructs. *Nano Today* **46**, 101584 (2022).

33. J. Ma, C. Qin, J. Wu, H. Zhuang, L. Du, J. Xu, C. Wu, 3D multicellular micropatterning biomaterials for hair regeneration and vascularization. *Mater. Horiz.* **10**, 3773–3784 (2023).

34. L. Du, C. Qin, H. J. Zhang, F. Han, J. M. Xue, Y. F. Wang, J. F. Wu, Y. Xiao, Z. G. Huan, C. T. Wu, Multicellular bioprinting of biomimetic inks for tendon-to-bone regeneration. *Adv. Sci.* **10**, 2301309 (2023).

35. C. Qin, H. Zhang, L. Chen, M. Zhang, J. Ma, H. Zhuang, Z. Huan, Y. Xiao, C. Wu, Cell-laden scaffolds for vascular-innervated bone regeneration. *Adv. Healthc. Mater.* **12**, e2201923 (2023).

36. J. Wu, C. Qin, J. Ma, H. Zhang, J. Chang, L. Mao, C. Wu, An immunomodulatory bioink with hollow manganese silicate nanospheres for angiogenesis. *Appl. Mater. Today* **23**, 101015 (2021).

37. S. Chae, Y. Sun, Y. J. Choi, D. H. Ha, I. Jeon, D.-W. Cho, 3D cell-printing of tendon-bone interface using tissue-derived extracellular matrix bioinks for chronic rotator cuff repair. *Biofabrication* **13**, abd159 (2021).

38. T. K. Merceron, M. Burt, Y. J. Seol, H. W. Kang, S. J. Lee, J. J. Yoo, A. Atala, A 3D bioprinted complex structure for engineering the muscle-tendon unit. *Biofabrication* **7**, 035003 (2015).

39. L. Chen, C. Deng, J. Li, Q. Yao, J. Chang, L. Wang, C. Wu, 3D printing of a lithium-calcium-silicate crystal bioscaffold with dual bioactivities for osteochondral interface reconstruction. *Biomaterials* **196**, 138–150 (2019).

40. H. Zhang, W. Ma, H. Ma, C. Qin, J. Chen, C. Wu, Spindle-like zinc silicate nanoparticles accelerating innervated and vascularized skin burn wound healing. *Adv. Healthc. Mater.* **11**, e2102359 (2022).

41. J. Ma, C. Qin, J. Wu, H. Zhang, H. Zhuang, M. Zhang, Z. Zhang, L. Ma, X. Wang, B. Ma, J. Chang, C. Wu, 3D printing of strontium silicate microcylinder-containing multicellular biomaterial inks for vascularized skin regeneration. *Adv. Healthc. Mater.* **10**, e2100523 (2021).

42. Q. Yu, J. Chang, C. Wu, Silicate bioceramics: From soft tissue regeneration to tumor therapy. *J. Mater. Chem. B* **7**, 5449–5460 (2019).

43. C. T. Wu, J. Chang, A review of bioactive silicate ceramics. *Biomed. Mater.* **8**, 032001 (2013).

44. A. M. Brokesh, A. K. Gaharwar, Inorganic biomaterials for regenerative medicine. *ACS Appl. Mater. Interfaces* **12**, 5319–5344 (2020).

45. F. B. Bagambisa, U. Joos, Preliminary studies on the phenomenological behaviour of osteoblasts cultured on hydroxyapatite ceramics. *Biomaterials* **11**, 50–56 (1990).

46. X. Z. Liu, Y. E. Li, S. Wang, M. K. Lu, J. Zou, Z. M. Shi, B. B. Xu, W. Wang, B. Hu, T. Jin, F. Wu, S. Liu, C. Y. Fan, PDGF-loaded microneedles promote tendon healing through p38/cyclin D1 pathway mediated angiogenesis. *Mater. Today Bio* **16**, 100428 (2022).

47. W. Y. Zhai, H. X. Lu, C. T. Wu, L. Chen, X. T. Lin, K. Naoki, G. P. Chen, J. Chang, Stimulatory effects of the ionic products from Ca-Mg-Si bioceramics on both osteogenesis and angiogenesis in vitro. *Acta Biomater.* **9**, 8004–8014 (2013).

48. L. L. Ouyang, J. P. K. Armstrong, Q. Chen, Y. Y. Lin, M. M. Stevens, Void-Free 3D bioprinting for in situ endothelialization and microfluidic perfusion. *Adv. Funct. Mater.* **30**, 1908349 (2020).

49. S. Zhang, W. Ju, X. Chen, Y. Zhao, L. Feng, Z. Yin, X. Chen, Hierarchical ultrastructure: An overview of what is known about tendons and future perspective for tendon engineering. *Bioact. Mater.* **8**, 124–139 (2022).

50. C. Shukunami, A. Takimoto, M. Oro, Y. Hiraki, Scleraxis positively regulates the expression of tenomodulin, a differentiation marker of tenocytes. *Dev. Biol.* **298**, 234–247 (2006).

51. D. Docheva, E. B. Hunziker, R. Fässler, O. Brandau, Tenomodulin is necessary for tenocyte proliferation and tendon maturation. *Mol. Cell. Biol.* **25**, 699–705 (2005).

52. A. Corsi, T. Xu, X. D. Chen, A. Boyde, J. Liang, M. Mankani, B. Sommer, R. V. Iozzo, I. Eichstetter, P. G. Robey, P. Bianco, M. F. Young, Phenotypic effects of biglycan deficiency are linked to collagen fibril abnormalities, are synergized by decorin deficiency, and mimic Ehlers-Danlos-like changes in bone and other connective tissues. *J. Bone Miner. Res.* **17**, 1180–1189 (2009).

53. G. Zhang, Y. Ezura, I. Chervoneva, P. S. Robinson, D. P. Beason, E. T. Carine, L. J. Soslowsky, R. V. Iozzo, D. E. Birk, Decorin regulates assembly of collagen fibrils and acquisition of biomechanical properties during tendon development. *J. Cell. Biochem.* **98**, 1436–1449 (2006).

54. S. Kalamajski, A. Aspberg, K. Lindblom, D. Heinegård, Å. Oldberg, Asporin competes with decorin for collagen binding, binds calcium and promotes osteoblast collagen mineralization. *Biochem. J.* **423**, 53–59 (2009).

55. K. Xu, Y. B. Shao, Y. Xia, Y. N. Qian, N. Jiang, X. Q. Liu, L. Yang, C. L. Wang, Tenascin-C regulates migration of SOX10 tendon stem cells via integrin-α9 for promoting patellar tendon remodeling. *Biofactors* **47**, 768–777 (2021).

56. S. Chae, U. Yong, W. Park, Y. M. Choi, I. H. Jeon, H. Kang, J. Jang, H. S. Choi, D. W. Cho, 3D cell-printing of gradient multi-tissue interfaces for rotator cuff regeneration. *Bioact. Mater.* **19**, 611–625 (2023).

57. P. Cheng, P. Han, C. Zhao, S. Zhang, H. Wu, J. Ni, P. Hou, Y. Zhang, J. Liu, H. Xu, S. Liu, X. Zhang, Y. Zheng, Y. Chai, High-purity magnesium interference screws promote fibrocartilaginous entheses regeneration in the anterior cruciate ligament reconstruction rabbit model via accumulation of BMP-2 and VEGF. *Biomaterials* **81**, 14–26 (2016).

58. M. Su, Q. Zhang, Y. Zhu, S. Wang, J. Lv, J. Sun, P. Qiu, S. Fan, K. Jin, L. Chen, X. Lin, Preparation of decellularized triphasic hierarchical bone-fibrocartilage-tendon composite extracellular matrix for enthesis regeneration. *Adv. Healthc. Mater.* **8**, e1900831 (2019).

59. Z. Chen, M. C. Jin, H. Y. He, J. B. Dong, J. Li, J. B. Nie, Z. C. Wang, J. T. Xu, F. Wu, Mesenchymal stem cells and macrophages and their interactions in tendon-bone healing. *J. Orthop. Transl.* **39**, 63–73 (2023).

60. Q. Zhou, W. Wang, F. J. Yang, H. Wang, X. D. Zhao, Y. Q. Zhou, P. L. Fu, Y. Z. Xu, Corrigendum: Disulfiram suppressed peritendinous fibrosis through inhibiting macrophage accumulation and its pro-inflammatory properties in tendon bone healing. *Front. Bioeng. Biotechnol.* **10**, 1054283 (2022).

61. D. Ma, J. Wang, M. Zheng, Y. Zhang, J. Huang, W. Li, Y. Ding, Y. Zhang, S. Zhu, L. Wang, X. Wu, S. Guan, Degradation behavior of ZE21C magnesium alloy suture anchors and their effect on ligament-bone junction repair. *Bioact. Mater.* **26**, 128–141 (2023).

62. M. E. Brown, J. L. Puetzer, Driving native-like zonal enthesis formation in engineered ligaments using mechanical boundary conditions and β-tricalcium phosphate. *Acta Biomater.* **140**, 700–716 (2022).

63. F. Han, T. Li, M. M. Li, B. J. Zhang, Y. F. Wang, Y. F. Zhu, C. T. Wu, Nano-calcium silicate mineralized fish scale scaffolds for enhancing tendon-bone healing. *Bioact. Mater.* **20**, 29–40 (2023).

64. X. P. Yu, Y. F. Wang, M. Zhang, H. S. Ma, C. Feng, B. J. Zhang, X. Wang, B. Ma, Q. Q. Yao, C. T. Wu, 3D printing of gear-inspired biomaterials: Immunomodulation and bone regeneration. *Acta Biomater.* **156**, 222–233 (2023).

65. B. Zhang, F. Han, Y. Wang, Y. Sun, M. Zhang, X. Yu, C. Qin, H. Zhang, C. Wu, Cells-micropatterning biomaterials for immune activation and bone regeneration. *Adv. Sci.* **9**, e2200670 (2022).

66. X. T. He, X. Li, M. Zhang, B. M. Tian, L. J. Sun, C. S. Bi, D. K. Deng, H. Zhou, H. L. Qu, C. Wu, F. M. Chen, Role of molybdenum in material immunomodulation and periodontal wound healing: Targeting immunometabolism and mitochondrial function for macrophage modulation. *Biomaterials* **283**, 121439 (2022).

67. H. Cheng, H. Huang, Z. Guo, Y. Chang, Z. Li, Role of prostaglandin E2 in tissue repair and regeneration. *Theranostics* **11**, 8836–8854 (2021).

68. J. Pajarinen, T. Lin, E. Gibon, Y. Kohno, M. Maruyama, K. Nathan, L. Lu, Z. Yao, S. B. Goodman, Mesenchymal stem cell-macrophage crosstalk and bone healing. *Biomaterials* **196**, 80–89 (2019).

69. Y. R. Na, D. Jung, M. Stakenborg, H. Jang, G. J. Gu, M. R. Jeong, S. Y. Suh, H. J. Kim, Y. H. Kwon, T. S. Sung, S. B. Ryoo, K. J. Park, J. P. Im, J. Y. Park, Y. S. Lee, H. Han, B. Park, S. Lee, D. Kim, H. S. Lee, I. Cleynen, G. Matteoli, S. H. Seok, Prostaglandin E$_2$ receptor PTGER$_4$-expressing macrophages promote intestinal epithelial barrier regeneration upon inflammation. *Gut* **70**, 2249–2260 (2021).

70. H. Chen, B. Hu, X. Lv, S. A. Zhu, G. H. Zhen, M. Wan, A. Jain, B. Gao, Y. Chai, M. Yang, X. Wang, R. X. Deng, L. Wang, Y. Cao, S. F. Ni, S. Liu, W. Yuan, H. J. Chen, X. Z. Dong, Y. Guan, H. L. Yang, X. Cao, Prostaglandin E2 mediates sensory nerve regulation of bone homeostasis. *Nat. Commun.* **10**, 181 (2019).

71. W. Qiao, D. Pan, Y. Zheng, S. Wu, X. Liu, Z. Chen, M. Wan, S. Feng, K. M. C. Cheung, K. W. K. Yeung, X. Cao, Divalent metal cations stimulate skeleton interoception for new bone formation in mouse injury models. *Nat. Commun.* **13**, 535 (2022).

72. O. Dolkart, T. Liron, O. Chechik, D. Somjen, T. Brosh, E. Maman, Y. Gabet, Statins enhance rotator cuff healing by stimulating the COX2/PGE2/EP4 pathway an in vivo and in vitro study. *Am. J. Sports Med.* **42**, 2869–2876 (2014).

73. P. Zhou, D. Xia, Z. Ni, T. Ou, Y. Wang, H. Zhang, L. Mao, K. Lin, S. Xu, J. Liu, Calcium silicate bioactive ceramics induce osteogenesis through oncostatin M. *Bioact. Mater.* **6**, 810–822 (2021).

74. H. Pan, L. Deng, L. Huang, Q. Zhang, J. Yu, Y. Huang, L. Chen, J. Chang, 3D-printed Sr$_2$ZnSi$_2$O$_7$ scaffold facilitates vascularized bone regeneration through macrophage immunomodulation. *Front. Bioeng. Biotechnol.* **10**, 1007535 (2022).

75. Y. Huang, C. Wu, X. Zhang, J. Chang, K. Dai, Regulation of immune response by bioactive ions released from silicate bioceramics for bone regeneration. *Acta Biomater.* **66**, 81–92 (2018).

76. A. I. Alford, K. D. Hankenson, Matricellular proteins: Extracellular modulators of bone development, remodeling, and regeneration. *Bone* **38**, 749–757 (2006).

77. Y. M. Bi, D. Ehirchiou, T. M. Kilts, C. A. Inkson, M. C. Embree, W. Sonoyama, L. Li, A. I. Leet, B. M. Seo, L. Zhang, S. T. Shi, M. F. Young, Identification of tendon stem/progenitor cells and the role of the extracellular matrix in their niche. *Nat. Med.* **13**, 1219–1227 (2007).